

A NIRCam-dark galaxy detected with the MIRI/F1000W filter in the MIDIS/JADES Hubble Ultra Deep Field

PABLO G. PÉREZ-GONZÁLEZ ,¹ PIERLUIGI RINALDI ,² KARINA I. CAPUTI ,² JAVIER ÁLVAREZ-MÁRQUEZ ,¹ MARIANNA ANNUNZIATELLA ,¹ DANIAL LANGEROODI ,³ THIBAUD MOUTARD ,⁴ LEINDERT BOOGAARD ,⁵ EDOARDO IANI ,² JENS MELINDER ,⁶ LUCA COSTANTIN ,¹ GÖRAN ÖSTLIN ,⁶ LUIS COLINA ,¹ THOMAS R. GREVE ,^{7,8,9} GILLIAN WRIGHT ,¹⁰ ALMUDENA ALONSO-HERRERO ,¹¹ ARJAN BIK ,⁶ SARAH E. I. BOSMAN ,^{12,13} ALEJANDRO CRESPO GÓMEZ ,¹ DANIEL DICKEN ,¹⁰ ANDREAS ECKART ,¹⁴ MACARENA GARCÍA-MARÍN ,¹⁵ STEVEN GILLMAN ,^{7,8} MANUEL GÜDEL ,^{16,17} THOMAS HENNING ,⁵ JENS HJORTH ,³ IRIS JERMANN ,^{7,8} ÁLVARO LABIANO ,¹⁸ ROMAIN A. MEYER ,¹⁹ FLORIAN PEIßKER ,¹⁴ JOHN P. PYE ,²⁰ THOMAS P. RAY ,²¹ TUOMO TIKKANEN ,²² FABIAN WALTER ,⁵ AND PAUL P. VAN DER WERF ,²³

¹Centro de Astrobiología (CAB), CSIC-INTA, Ctra. de Ajalvir km 4, Torrejón de Ardoz, E-28850, Madrid, Spain

²Kapteyn Astronomical Institute, University of Groningen, P.O. Box 800, 9700 AV Groningen, The Netherlands

³DARK, Niels Bohr Institute, University of Copenhagen, Jagtvej 155, 2200 Copenhagen, Denmark

⁴European Space Agency (ESA), European Space Astronomy Centre (ESAC), Camino Bajo del Castillo s/n, 28692 Villanueva de la Cañada, Madrid, Spain

⁵Max Planck Institut für Astronomie, Königstuhl 17, D-69117, Heidelberg, Germany

⁶Department of Astronomy, Stockholm University, Oscar Klein Centre, AlbaNova University Centre, 106 91 Stockholm, Sweden

⁷Cosmic Dawn Center (DAWN), Denmark

⁸DTU Space, Technical University of Denmark, Elektrovej, Building 328, 2800, Kgs. Lyngby, Denmark

⁹Dept. of Physics and Astronomy, University College London, Gower Street, London WC1E 6BT, United Kingdom

¹⁰UK Astronomy Technology Centre, Royal Observatory Edinburgh, Blackford Hill, Edinburgh EH9 3HJ, UK

¹¹Centro de Astrobiología (CAB), CSIC-INTA, Camino Bajo del Castillo s/n, E-28692 Villanueva de la Cañada, Madrid, Spain

¹²Institute for Theoretical Physics, Heidelberg University, Philosophenweg 12, D-69120, Heidelberg, Germany

¹³Max-Planck-Institut für Astronomie, Königstuhl 17, 69117 Heidelberg, Germany

¹⁴I.Physikalisches Institut der Universität zu Köln, Zülpicher Str. 77, 50937 Köln, Germany

¹⁵European Space Agency, Space Telescope Science Institute, Baltimore, Maryland, USA

¹⁶Dept. of Astrophysics, University of Vienna, Türkenschanzstr 17, A-1180 Vienna, Austria

¹⁷ETH Zürich, Institute for Particle Physics and Astrophysics, Wolfgang-Pauli-Str. 27, 8093 Zürich, Switzerland

¹⁸Telespazio UK for the European Space Agency, ESAC, Camino Bajo del Castillo s/n, 28692 Villanueva de la Cañada, Spain

¹⁹Department of Astronomy, University of Geneva, Chemin Pegasi 51, 1290 Versoix, Switzerland

²⁰School of Physics & Astronomy, Space Research Centre, Space Park Leicester, University of Leicester, 92 Corporation Road, Leicester, LE4 5SP, UK

²¹Dublin Institute for Advanced Studies, 31 Fitzwilliam Place, D02 XF86, Dublin, Ireland

²²School of Physics & Astronomy, Space Research Centre, Space Park Leicester, University of Leicester, 92 Corporation Road, Leicester, LE4 5SP, UK

²³Leiden Observatory, Leiden University, P.O. Box 9513, 2300 RA Leiden, The Netherlands

ABSTRACT

We report the discovery of *Cerberus*, an extremely red object detected with the MIRI Deep Imaging Survey (MIDIS) observations in the F1000W filter of the Hubble Ultra Deep Field. The object is detected at $S/N \sim 6$, with $F1000W \sim 27$ mag, and it is extremely faint in both the NIRCam data gathered by the JWST Advanced Deep Extragalactic Survey, JADES, with ~ 30.5 mag 5σ upper limits in individual bands, as well as in the MIDIS F560W ultra deep data (~ 29 mag, 5σ). Analyzing the spectral energy distribution built with individual (low S/N) optical-to-mid-infrared filters and ($S/N \sim 5$) stacks, we discuss the possible nature of this red NIRCam-dark source using a battery of codes. We discard the possibility of *Cerberus* being a Solar System body based on the $< 0''.016$ proper motion in the 1-year apart JADES and MIDIS observations. A sub-stellar Galactic nature is deemed unlikely, given that the *Cerberus*' relatively flat NIRCam-to-NIRCam and very red NIRCam-to-MIRI flux ratios are not consistent with any brown dwarf model. The extragalactic nature of *Cerberus* offers 3 possibilities: (1) A $z \sim 0.4$ galaxy with strong emission from polycyclic aromatic hydrocarbons; the

very low inferred stellar mass, $M_\star = 10^{5-6} M_\odot$, makes this possibility highly improbable. (2) A dusty galaxy at $z \sim 4$ with an inferred stellar mass $M_\star \sim 10^8 M_\odot$. (3) A galaxy with observational properties similar to those of the reddest little red dots discovered around $z \sim 7$, but *Cerberus* lying at $z \sim 15$, presenting a spectral energy distribution in the rest-frame optical dominated by emission from a dusty torus or a dusty starburst.

Keywords: Galaxy formation (595) — Galaxy evolution (594) — High-redshift galaxies (734) — Stellar populations (1622) — Broad band photometry (184) — Galaxy ages (576) — JWST (2291) — Active galactic nuclei (16)

1. INTRODUCTION

Building increasingly powerful telescopes operating at redder and redder wavelengths and (unexpectedly) discovering new types of galaxies at higher and higher redshifts is a classical industry now, established nearly 40 years ago. Indeed, deep optical surveys carried out in the late twentieth century using highly sensitive detectors were found to miss interesting galaxy populations of evolved and dust-rich galaxies at cosmological distances, both types being relatively bright at near-infrared wavelengths and easily detectable by new instruments, even though they were significantly less efficient in detecting photons and were affected by much larger backgrounds. The key for their discovery was large (red) colors (flux density ratios typically larger than an order of magnitude) between a near-infrared and an optical band, i.e., they were extremely red objects.

The first Extremely Red Objects (EROs) were reported using new ground-based near-infrared telescopes built nearly 40 years ago. They were found to be members of cosmologically relevant galaxy populations, comprising a variety of galaxies ranging from high redshift quasars to very young and dust-rich galaxies, or even “high” redshift passive galaxies (see, among many, Elston et al. 1988; McCarthy 2004; Graham & Dey 1996; Franx et al. 2003; Pozzetti & Mannucci 2000).

With the development of very sensitive instruments in space telescopes such as *Spitzer*, the search was moved to longer wavelengths in the mid-infrared, at first compared with optical datasets (Wilson et al. 2004; Yan et al. 2004).

Remarkably, when the *Hubble* Space Telescope gathered extremely deep data taken in the near-infrared up to $1.6 \mu\text{m}$, with surveys such as CANDELS or the WFC3 Hubble Ultra Deep Field (Koekemoer et al. 2011; Grogin et al. 2011; Koekemoer et al. 2013), *Spitzer*/IRAC data were still shown to detect unique distinctively red objects which were only visible at wavelengths longer than $3 \mu\text{m}$, or at least were extremely faint in the near-infrared and optical spectral ranges. These so-called HST-dark galaxies were studied for around a

decade, with significant uncertainties about their nature due to the strong sensitivity limitations of our multi-wavelength telescopes, even those operating in very different observational windows such as the (sub-)millimeter range (see, e.g., Franco et al. 2018; Alcalde Pampliega et al. 2019; Wang et al. 2019). JWST has started, from the earliest phases of the mission, to shed light on those HST-dark galaxies, i.e., mid-infrared bright near-infrared/optically faint sources which now constitute the bulk of the JWST galaxy exploration (Pérez-González et al. 2023a; Barrufet et al. 2023; Williams et al. 2023a; Gillman et al. 2023).

The ERO astrophysical industry is intimately tied to the discovery of submillimeter galaxies (SMGs, Hughes et al. 1998). Indeed, many EROs are dusty starbursts, which appear in mid- and far-infrared surveys in different flavors and with different names, starting from SMGs (see, e.g., Blain et al. 2002; Chapman et al. 2005) but also (hot) dust-obsured galaxies (DOGs, Dey et al. 2008; Narayanan et al. 2010; hotDOGs, Tsai et al. 2015), extremely red quasars (ERQ, Hamann et al. 2017), or, more descriptive from an observational point of view, (ultra-)luminous infrared galaxies (U/LIRGs, Sanders & Mirabel 1996; Elbaz et al. 2002; Pérez-González et al. 2005; Le Floc'h et al. 2005; Caputi et al. 2007; Magnelli et al. 2009; Madau & Dickinson 2014).

Last but not least, EROs, especially if selected at the faintest magnitudes and with appropriate bands for the color, overlap with very high-redshift galaxy samples selected using the Lyman break technique (Steidel et al. 1996) at higher and higher redshifts (e.g., Bouwens et al. 2011).

Remarkably, with the advent of JWST, both industries, searching for red objects and for those with higher and higher redshifts, have been merged at a profound level, with the possibility of finding double-break (Lyman and Balmer) red galaxies, now known as little red dots (Labbé et al. 2023a; Matthee et al. 2023; Barro et al. 2023; Pérez-González et al. 2024), or high redshift galaxies with very high equivalent width emission lines, first discovered with *Spitzer* (Smit et al. 2014), now ap-

pearing in many JWST works (Pérez-González et al. 2023a; Rinaldi et al. 2023). Interestingly, some of these sources have been confirmed to present broad emission line components possibly linked to an active galactic nucleus (AGN; Kocevski et al. 2023; Greene et al. 2023).

The interesting subtopics of finding and characterizing dusty galaxies on the one hand, and high redshift galaxy candidates on the other, has been demonstrated to be very relevant for JWST surveys, which can easily misidentify one type of galaxy with the other (see, e.g., Zavala et al. 2023; Naidu et al. 2022).

The MIRI instrument onboard the JWST (Rieke et al. 2015; Wright et al. 2023) now offers the possibility to search for red galaxies with longer color baselines, beyond the wavelengths first probed by *Spitzer*/IRAC and now easily accessible with impressive depths (~ 30 mag and beyond) using JWST/NIRCam. Even though MIRI cannot reach NIRCam depths, very deep imaging at $5.6 - 12.8 \mu\text{m}$ reaching magnitudes around 27–29 is already available and opens a whole new window for the search and characterization of high redshift galaxies (Papovich et al. 2023; Barro et al. 2023; Rinaldi et al. 2023; Pérez-González et al. 2024).

In this paper, we report the discovery of a MIRI-bright red object appearing in the MIRI Deep Imaging Survey (MIDIS) F1000W imaging of the Hubble Ultra Deep Field (Östlin et al., 2024, in prep.). The source is extremely faint at NIRCam long wavelengths, i.e., it is a NIRCam-dark object lying at the edge of the detection limit (~ 30.5 mag) of one of the deepest JWST surveys available to date, JADES (Eisenstein et al. 2023a), having not been catalogued before (Rieke et al. 2023; Eisenstein et al. 2023b). Consequently, our object presents an extremely red color between 4.4 and $10 \mu\text{m}$, and, in fact, the source is also red with respect to the bluest MIRI filter, as revealed by the MIDIS F560W imaging.

This letter is organized as follows. Section 2 presents the deep MIRI data used in this letter, as well as ancillary observations taken with NIRCam, ALMA, and VLT. Section 3 describes our method to detect NIRCam-dark galaxies, and the case for a positive detection in the Hubble Ultra Deep Field, the source we call *Cerberus*. Section 4 presents the spectral energy distribution of *Cerberus* and discusses the several possible interpretations, analyzing the implied physical properties for each one of them. Finally, Section 5 presents a summary of our findings.

Throughout the paper, we assume a flat cosmology with $\Omega_M = 0.3$, $\Omega_\Lambda = 0.7$, and a Hubble constant $H_0 = 70 \text{ km s}^{-1} \text{Mpc}^{-1}$. We use AB magnitudes (Oke & Gunn 1983). All stellar mass and SFR estimations as-

sume a universal Chabrier (2003) initial mass function (IMF), unless stated otherwise.

2. THE MIRI DEEP F1000W SURVEY IN THE HUDF, AND ANCILLARY DATA

2.1. *MIRI* data

MIRI data in the F1000W filter were taken as part of the MIRI Deep Imaging Survey (MIDIS, Östlin et al. 2024, in prep.) in December 2023. The observation consisted of 11 exposures, each with 100 groups, FASTR1 readout, and 10 integrations, for a total on source exposure time of 30800 s, centered on the Hubble Ultra Deep Field (HUDF). The dithering pattern was set to large-size cycling, with the 11 exposures taken in different positions on the sky separated by up to $10''$. We remark that the dithering pattern, with no repeated positions, is very important for the detection of faint sources, such as the one presented here, and their distinction from detector artifacts.

The reduction of the MIRI data followed the methodology described in Pérez-González et al. (2024). Briefly, a super-background strategy is used to build background maps for each single image using all the other exposures (since they were taken during the same campaign), which results in a very homogeneous background (in terms of level and noise). Known sources are masked to avoid biasing the determination of the very local background in the super-background frame. Our F1000W image, reduced with a 60 milliarcsec pixels, presents an average 5σ depth of 26.8 mag, measured in an $r=0''.4$ circular aperture, and taking into account a 30% aperture correction as well as noise correlation.

We present the MIDIS F1000W data in Figure 1 with an RGB image built in combination with some NIRCam long wavelength data.

2.2. *Ancillary* data

In this subsection, we describe other datasets in the HUDF that we have used to complement the MIRI data.

2.2.1. *Other MIRI* data

For this letter, we combined the recently acquired MIDIS F1000W data with the F560W ultra-deep observations also carried out by MIDIS in December 2022. These data are described in Östlin et al. (2024, in prep.) and consist of ~ 40 hours on source taken in the HUDF, which allowed us to reach 28.7 mag 5σ for point-like sources measured in an $r=0''.23$ circular aperture.

2.2.2. *NIRCam* data

The MIRI/F1000W data were also complemented with NIRCam imaging taken by the JWST Advanced

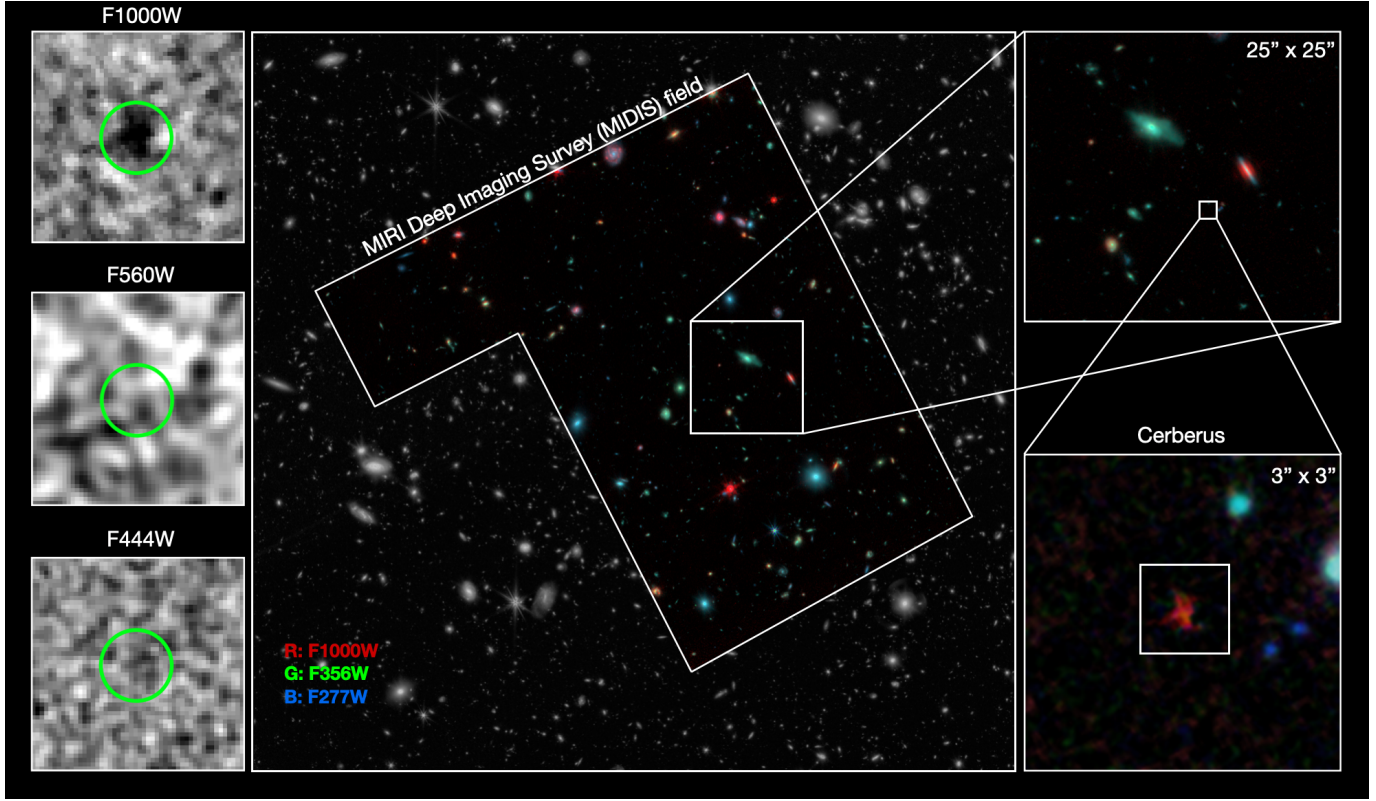


Figure 1. In the center of the figure, we show an RGB composition of the MIDIS F1000W field. The color images have been built with JADES data in 2 NIRCam filters, F277W and F356W, and the MIDIS MIRI F1000W filter (all images convolved to the same PSF of MIRI/F1000W). In the background, we show the HUDF JADES data in grayscale. We provide a series of zoomed-in RGB frames that lead to the NIRCam-dark MIRI source, *Cerberus*, whose image is located at the bottom right corner. The NIRCam-dark MIRI source *Cerberus* is highlighted with a square in that RGB frame. Additionally, we provide postage stamp images ($2'' \times 2''$) of *Cerberus* in MIRI/F1000W, MIRI/F560W, and NIRCam/F444W (left column), showcasing that *Cerberus* (marked with an $r=0''.25$ green circle) is clearly detected only at $10 \mu\text{m}$.

Deep Extragalactic Survey, JADES (Eisenstein et al. 2023a), Data Release 2 (Eisenstein et al. 2023b), which includes also observations from the JWST Extragalactic Medium-band Survey (JEMS, Williams et al. 2023b) and the First Reionization Epoch Spectroscopically Complete Observations (FRESCO, Oesch et al. 2023). This dataset provides a total of 14 bands from 0.9 to $4.8 \mu\text{m}$ (6 at short-wavelength, SW, and 8 at long-wavelength, LW), with 5σ depths ranging from 30.5 to 30.9 mag (measured in a $0''.2$ radius circular apertures). We remark that JADES is one of the deepest NIRCam surveys on the sky, only matched in depth (in some bands) by the MIDIS NIRCam-parallel project (Pérez-González et al. 2023b) and The Next Generation Deep Extragalactic Exploratory Public Near-Infrared Slitless Survey, NGDEEP (Bagley et al. 2023), which means that our search for NIRCam-dark galaxies is really probing the current depth limitations of JWST extragalactic surveys.

2.2.3. ALMA data

The Atacama Large Millimeter/submillimeter Array (ALMA) Spectroscopic Survey in the Hubble Ultra Deep Field (ASPECS) is a Cycle 4 Large Program over a 4.6 arcmin^2 scan at 1.2 mm (Decarli et al. 2020; González-López et al. 2020) and 3.0 mm (Decarli et al. 2019; González-López et al. 2019). By covering a broader area and offering complementary data on spectral lines and redshifts, these surveys have progressively enhanced our understanding of the cosmic molecular gas density up to a redshift of approximately $z \approx 4$. The ultra-deep 1.2 mm data reaches an rms sensitivity of $9.3 \mu\text{Jy}/\text{beam}$, with beam dimensions of $1''.5 \times 1''.1$. The 3.0 mm data reaches $1.4 \mu\text{Jy}/\text{beam}$, with a $1''.8 \times 1''.5$ beam.

2.2.4. MUSE data

The HUDF has been extensively studied in the last decade with the Multi Unit Spectroscopic Explorer (MUSE, Bacon et al. 2010) mounted on the Very Large Telescope (VLT) as part of the MOSAIC and UDF-10 fields (GTO programs 094.A- 0289(B), 095.A-0010(A), 096.A-0045(A) and 096.A- 0045(B), PI: R. Bacon) and

the most recent MXDF observations (GTO Large Program 1101.A-0127, PI: R. Bacon). More details about these programs can be found in [Bacon et al. \(2017, 2023\)](#).

Briefly, MOSAIC, UDF-10, and MXDF covered the Hubble eXtreme Deep Field (XDF) within HUDF with MUSE observations in Wide-Field Mode (WFM) with each single pointing covering an area of about 1 arcmin², with a spectral wavelength range between 4700 - 9300 Å and a spectral resolving power (R) that varies from 1770 (4800 Å) to 3590 (9300 Å). The UDF-10 and MOSAIC programs were carried out without employing the ground-layer adaptive optics mode provided by the VLT Adaptive Optics Facility (AOF) and its GALACSI adaptive optics module, as detailed in [Kolb et al. \(2016\)](#) and [Madec et al. \(2018\)](#). In contrast, the MXDF program leveraged the capabilities of VLT’s AOF along with the GALACSI module to enhance its observations.

By using the WFM mode, MUSE achieves a spatial sampling of $0.^{\prime\prime}2 \times 0.^{\prime\prime}2$. However, the spatial resolution experienced notable variation across the different programs, with a median value of approximately $0.^{\prime\prime}8$ for the MOSAIC and UDF-10 programs, improving to $0.^{\prime\prime}4$ for the MXDF observations.

In the XDF region, which is covered by the MIDIS field, observations have achieved depths exceeding 140 hours, although the distribution of the depth in flux is not uniform across the area.

For this letter, we used the fully reduced MUSE datacubes for the MOSAIC + UDF-10 and MXDF programs, as well as the catalog of detected sources and corresponding redshifts that can be found in [Bacon et al. \(2023\)](#).

3. SELECTION AND VALIDATION OF NIRCAM-DARK SOURCES

This letter presents a source that was discovered on the MIDIS F1000W image and found to be missed by published catalogs ([Rieke et al. 2023; Eisenstein et al. 2023b](#)). In this section, we describe the selection procedure for such types of NIRCam-dark sources.

3.1. Selection of NIRCam-dark sources

In order to select NIRCam-dark sources, we executed the SExtractor software ([Bertin & Arnouts 1996](#)) directly using the MIRI/F1000W as the detection image. We followed the hot-mode extraction described in [Galametz et al. \(2013\)](#), which is particularly effective for detecting extremely faint sources.

Once we had a hot MIRI/F1000W catalog, we anti cross-matched it (using a $0.^{\prime\prime}3$ search radius) with the official JADES DR2 catalog published by [Eisenstein et al.](#)

(2023b, which superseded the DR1 catalog), constructed by selecting sources in a LW stack. The goal of the anti cross-match was to isolate sources uniquely detected by MIRI/F1000W. The result was a list of 17 *potential* NIRCam-dark sources selected at $10 \mu\text{m}$.

We meticulously examined each of the *potential* NIRCam-dark sources in the final mosaic to rule out the presence of an unflagged cosmic ray or any kind of hot and/or bad pixels that could have caused a spurious detection. We remark here that we have utilized 11 different exposures in the MIDIS F1000W survey, so the final mosaic should be free of most of these artifacts if the outlier rejection of the JWST pipeline works properly.

Visual inspection of the individual exposures revealed that for 16 of the 17 candidates, there was indeed a hot pixel in one of the 11 exposures which had survived the stacking process performed to produce the final mosaic (i.e., stage 3 of the official pipeline). We automated and generalized the source validation methodology by producing stacked mosaics with a limited number of exposures, excluding 1, 2, or 3 random frames. This procedure, obviously, affects the depth. Explaining the latter case in more detail as an example, we started from our collection of 11 `*.cal.fits` files, and we created the 165 unique mosaics which can be obtained by excluding sets of 3 `*.cal.fits` files for each partial mosaic. After building the 165 realizations, we inspected the 17 *potential* NIRCam-dark sources, concluding that only one source consistently appeared in all 165 different partial mosaics. The remaining candidates were found to vanish in some of the realizations, in fact even in the mosaics built excluding one single exposure, indicating their most-likely spurious nature. To further validate these findings, we made an in-depth analysis of each `*.cal.fits` file, confirming the presence of unflagged hot and/or bad pixels in some of them that indeed led to false detections in a number of the realizations.

One source of the 17 pre-selected candidates did not vanish in any of the partial mosaics, even when removing 3 random images. For this source, we measured photometry in a small $r=0.^{\prime\prime}25$ aperture (which maximized S/N on the partial mosaics), as well as the sky noise in a square $3.^{\prime\prime} \times 3.^{\prime\prime}$ region around, on all the mosaics produced by excluding 1, 2, and 3 exposures. We found consistent photometry and a degradation of the S/N consistent with the differences in exposure time. For example, for the skip-3 mosaics, we found an average magnitude 27.05 ± 0.19 mag, consistent with our measurement in the full mosaic (see Section 4). However, we found 2 contiguous exposures, numbers 7 and 8, which, if removed, produced a dimming of the source to 27.4 mag, still within 2σ of the measurement using

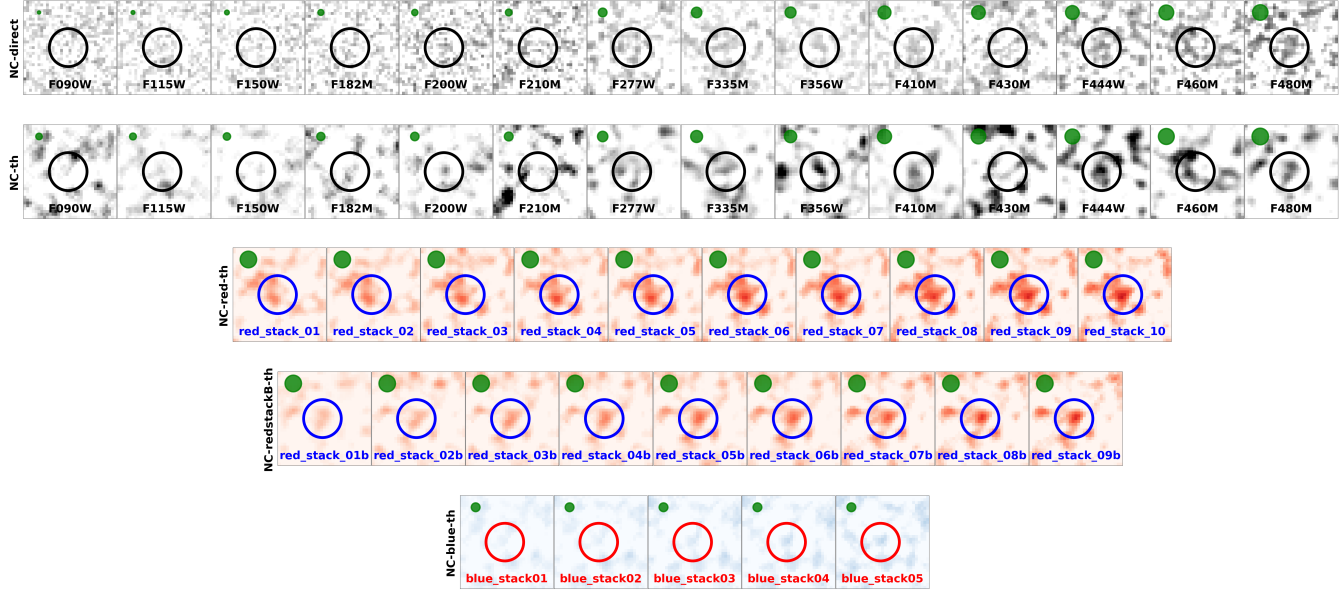


Figure 2. In the top row, we show postage stamps of *Cerberus* in all NIRCam bands from the JADES DR2 (Eisenstein et al. 2023b). The second row shows the same stamps but convolved with a 2-pixel radius tophat filter. The third row shows incremental stacks of NIRCam filters, starting from the reddest two bands (F480M and F460M) and adding one band at a time, down to F210M. The fourth row shows similar stacks, but avoiding F460M, which presents an artifact (see main text for details). The fifth row shows stacks starting from the bluest bands (blue_stack01 including F090W and F115W) and adding the next filter in subsequent images. All postage stamps are $1'' \times 1''$, with the source marked with a circle of radius $0''.2$. Green circles show the PSF FWHM (including the tophat filter).

the full dataset. We examined these exposures in detail and found no signs of a cosmic ray hit, but a slightly enhanced signal in an extended region which could be due to the general properties of the detector (which consistently showed a dimmer region in the super-background frames for all images) or a cosmic ray shower. Given that the two relatively (and slightly) brighter images were contiguous, we do not rule out transient behavior of the source or of some detector effect. Based on the persistence of the signal from the source in all partial stacks of the MIRI F1000W dataset, we concluded that it was not spurious.

The NIRCam-dark source we identified with this methodology was dubbed *Cerberus*, to acknowledge that it is a weird beast lurking in the darkest corners of the JWST surveys and with different interpretations/heads for its nature, as will be shown in Section 4. Its coordinates (J2000) are $\alpha = 03:32:38.09$ (hours), $\delta = -27:47:11.81$ (degrees). An RGB image of the source built with NIRCam and MIRI data is presented in Figure 1, jointly with postage stamps ($2'' \times 2''$) in the NIRCam/F444W, MIRI/F560W, and MIRI/F1000W filters.

3.2. Multi-wavelength validation and observational properties of the NIRCam-dark object *Cerberus*

In order to further validate and characterize *Cerberus*, we searched for detections in the datasets described in

Section 2, more specifically in the ultra-deep observations (among or even the deepest on the sky) provided by JWST/NIRCam, ALMA, and VLT/MUSE.

Directly linked to our selection criteria, the NIRCam-dark *Cerberus* object was not present in any of the catalogs of the JADES NIRCam survey (Rieke et al. 2023; Eisenstein et al. 2023b). We then proceeded to force photometric measurements in all bands (described in Section 4) and stacked several sets of images to probe any possible low-level signal present in the images. Figure 2 provides postage stamps of the source in all JADES NIRCam bands as well as in the stacks.

The 2 rows of greyscale stamps (one presenting direct images, another one showing data convolved with a 2-pixel radius tophat filter to enhance faint signal) show no clear detection of *Cerberus* in any band except F460M. The brightest knot observed within a $0''.2$ radius circular aperture in that band is remarkably compact, so we decided to investigate its possible spurious nature following the same procedure as for the F1000W data, i.e., producing partial-dataset stacks. We reduced the JEMS data ourselves and found that one of the 12 images presented a single hot pixel that survived the stacking process. Indeed, in the 220 different realizations of the NIRCam/F460M dataset we built by excluding 3 random `*.cal.fits` files, the signal disappeared in all

combinations excluding this frame. We decided to exclude this band from further analysis of *Cerberus*, since the central signal was also found to present an unusual shape. For the rest of the bands, we ran SExtractor using a more aggressive approach than what was used for the MIRI/F1000W data. Notwithstanding this, we were not able to detect anything at that position, except in the F460M band.

The 2 rows of postage stamps in Figure 2 shown with a red-palette and with our source marked with a blue circle depict incremental stacks constructed by averaging NIRCam bands starting from the reddest (convolved with a tophat kernel). The image on the left-end of the first row of these stamps combines F480M and F460M, the second adds F444W to the previous, the next one adds F430M, etc., and so forth. The final image adds all NIRCam bands from F182M to F444W. The second row of red stamps excludes F460M from the stacks, given the confirmed spurious nature of part of the signal in that filter. When we ran SExtractor, adopting the same aggressive method as for the individual NIRCam bands, we actually detected the source precisely at the location of our initial MIRI-detected NIRCam-dark candidate selected at $10\ \mu\text{m}$. The detection presents $S/N \gtrsim 5$ and it is compatible with a point-like source (but see discussion about morphology below). This test definitively demonstrated the existence of our MIRI-selected NIRCam-dark source, showing that this elusive source has a counterpart observable in the NIRCam bands exclusively by stacking very deep data, i.e., it lies near the detection limit of the JADES dataset (which is among or possibly even the deepest on the sky, jointly with MIDIS and NGDEEP, as we previously remarked).

The row presenting blue-palette stamps in Figure 2 shows stacks of NIRCam images starting from the bluest and adding one filter at a time. The image on the left-end of the row corresponds to F090W+F115W, then F150W is added, etc, and the last image includes all SW filters up to F210M. The source is much fainter in these blue stacks, some signal at the $S/N \sim 2$ level is tentatively detected in the last stack (see Section 4).

Apart from the incremental NIRCam stacks, in the following section we will use four sets of disjoint stacks, combining 2, 3, 4 and 5 bands, always starting from the reddest and not repeating them in different stacks of the same set. These stacks provided $S/N \sim 5$ detections in the 2-band set, specifically in the F480M+F444W (30.0 mag) and F356W+F335M (30.6 mag) combinations, and in one 3-band stack, the one combining F410M+F356W+F335M (30.5 mag).

Figure 3 shows a stacked NIRCam image (including all filters at $\lambda > 3\mu\text{m}$) convolved to the resolution of the

F1000W data (FWHM=0''.328). Each calibrated individual NIRCam filter was rebinned to a 0''.06 pixel scale and PSF-matched to F1000W using WebbPSF (v. 1.2.1 Perrin et al. 2014) models and the method described in Melinder et al. (2023), and then median-stacked. We measured the centroid of the source for both JWST instruments (using `photutils` with a circular footprint of 3 pixels radius), finding an agreement within 0.26 pixels, i.e., 0''.016. Remarkably, the source is slightly extended to the NW in both images. The morphology of the source is similar for the NIRCam stack and the MIRI F1000W image, with a tadpole-like shape extending to the upper right, further strengthening the positive detection of the source with NIRCam. We also notice a qualitative resemblance between the structure of *Cerberus* and GN-z11 (Oesch et al. 2016; Tacchella et al. 2023), with a concentrated flux distribution identified with the core of the galaxy and an extended haze component.

For the MUSE data, we made use of the recent MXDF observations that cover the XDF area with observations in WFM mode for a total of more than 140 hours (see Bacon et al. 2023, for more details). We downloaded the publicly available fully reduced MUSE data, as well as a catalogue of detected sources and corresponding spectroscopic redshifts¹. We extracted the MUSE 1D spectrum at the coordinates of our target within circular apertures of different sizes (0''.4 and 0''.8 radius) but found no significant spectral feature at the position of the NIRCam-dark candidate. This is also confirmed by the publicly available catalogue of detected sources by Bacon et al. (2023).

We also looked for emission lines in the MUSE data in the neighborhood of our source. We detected extended Ly α emission from a nearby source lying at $z \approx 4.77$ and celestial coordinates $\alpha = 03:32:37.95$ (hours), $\delta = -27:47:11.14$ (degrees). This source is reported by Bacon et al. (2023) with ID53. Interestingly, according to Bacon et al. (2023), there is Ly α emission associated with another source (ID7666), that we do not detect in the MXDF datacube, at $z \approx 4.14$ with celestial coordinates $\alpha = 03:32:38.08$ (hours), $\delta = -27:47:12.71$ (degrees). Both objects are at an angular separation of less than 1'' from our target.

Searching for a detection at (sub-)millimeter wavelengths, we made use of the deep ALMA dust continuum imaging from the ASPECS program at 1.2 mm and 3.0 mm that covers the HUDF. By carefully inspecting

¹ The MUSE cube and catalogue of sources can be found at the following link: <https://amused.univ-lyon1.fr/project/UDF/HUDF/>.

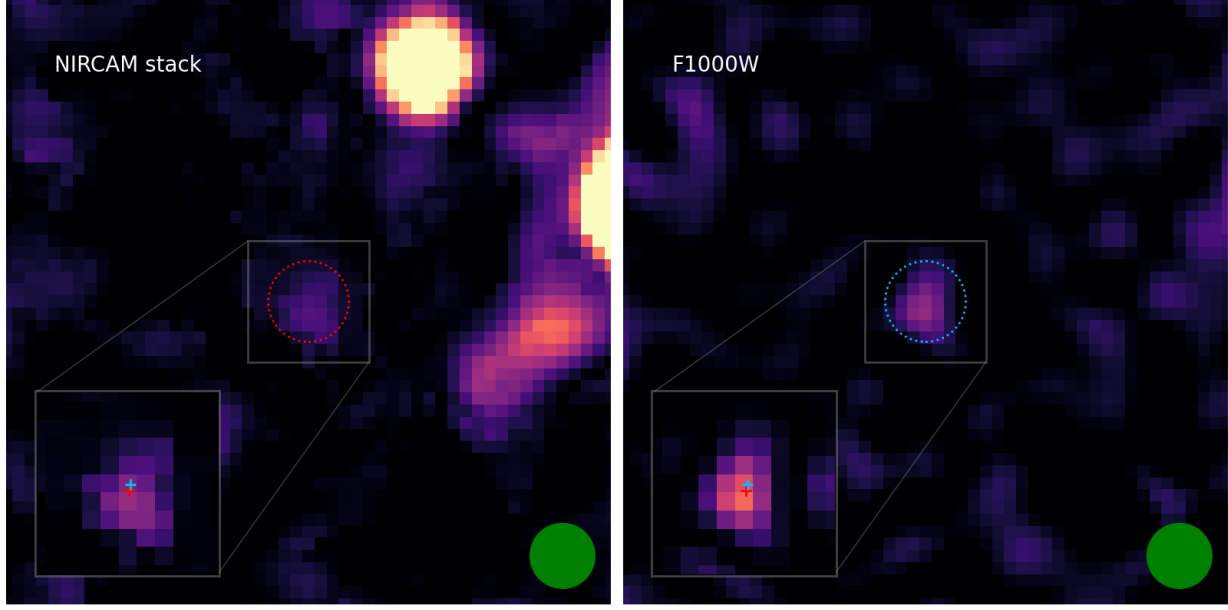


Figure 3. Stacked NIRCam (left panel) and MIRI/F1000W (right panel) images of the region around *Cerberus*. The stacked NIRCam image was produced from individually PSF matched LW images. Note that the spurious pixels in the F460M image (see text for details) is removed in the median stacking procedure. The angular size of the images and zoomed inset is $3'' \times 3''$ and $0''.6 \times 0''.6$, respectively. The red (blue) circle shows the location of the detected source in F1000W and has a radius of $0''.2$. The green filled circle shows the resolution of the F1000W image (with a diameter of $0''.328$). In the zoomed insets, we also show the centroid positions with the blue and red crosses, corresponding to the F1000W image and the NIRCam stack, respectively.

these maps, the source is not detected at either wavelength. This finding implies 3σ upper limits on the flux density at 1.2 mm and 3.0 mm of $27.9 \mu\text{Jy}$ and $4.2 \mu\text{Jy}$ respectively, assuming it is effectively an unresolved point-like source. Figure 4 presents the images of *Cerberus* in the ALMA 1.2 and 3 mm bands.

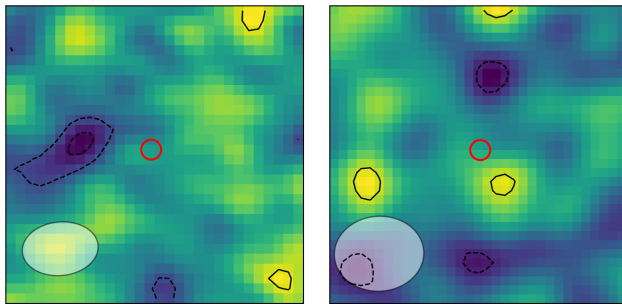


Figure 4. ALMA $6'' \times 6''$ cutouts at 1.2 mm and 3.0 mm from ASPECS. Contours are drawn at 1σ intervals starting at $\pm 2\sigma$ (dashed lines show negative contours). The source position is indicated with $0''.2$ radius circle. The beam size is shown in the bottom left corner. The source is not detected at either wavelength.

4. SPECTRAL ENERGY DISTRIBUTION ANALYSIS OF *CERBERUS*

4.1. *Multi-wavelength Photometry*

A spectral energy distribution (SED) for *Cerberus* was built by measuring photometry in all available NIRCam (including both individual bands and stacks) and MIRI bands. Given the faint and small nature of our source, we measured photometry in several circular apertures with radii ranging from $0.1''$ to $0.6''$. We measured the background in a small square region around *Cerberus* ($3''$ on the side) and calculated the noise using non-adjacent pixels (5 pixels apart) to take into account noise correlation, as explained in Pérez-González et al. (2023b).

All NIRCam SW measurements provided S/N values lower than 2. The 5σ depths for point-like sources of the 6 SW filters range from 29.6 mag for F090W to 30.6 mag for F200W, measured in each case with an aperture enclosing 65% of the encircled energy ($\sim 0''.1$ radius).

The measurements in the NIRCam LW channels presented $S/N < 5$ for all apertures, only the F277W and F460M filters approached that limit. For these bands, we obtained 31.16 ± 0.28 mag and 29.31 ± 0.23 mag (after removing the cosmic-ray artifact mention in Section 2), respectively, measured in a $0''.2$ radius aperture, and accounting for an ~ 0.3 mag aperture correction. Lower significances but near the $S/N = 5$ limit were obtained in F335M, F410M, F444W, and F480M, 30.80 ± 0.35 mag,

30.39 ± 0.40 mag, 30.91 ± 0.34 mag, and 29.59 ± 0.34 mag, respectively.

Given our magnitude measurement in the F1000W band, 27.13 ± 0.17 mag, obtained with photometry in an aperture of radius $0''.3$, which maximizes the S/N , we infer a very red color, $F444W - F1000W = 3.8 \pm 0.4$ mag.

These measurements and the stamps provided in Figure 2 show that *Cerberus* is barely detected in any individual NIRCam band, consistent with being around or below the 5σ detections limits, quoted to be around 30.5 – 31.0 mag for the JADES DR2 data (Eisenstein et al. 2023a). We remark that the F460M filter, which provides the brightest magnitude, presents a group of 4 pixels to the North of the position of our galaxy, which we confirmed to be an artifact of the reduction, and it is not seen in any other band (even the ones with deeper limiting magnitudes).

Figure 2 also shows stacked NIRCam data for *Cerberus*. Visually, it seems clear that there is signal at that sky position. We measured photometry in the same apertures used for the individual bands, assigning average aperture corrections for the filters included in each stack. The 5 LW stacks with the highest number of bands all provide $S/N > 5$ fluxes (the average being $S/N \sim 6$), ranging from 30.3 to 30.8 mag. This means that the (low- S/N) SED is characterized by a red color extending through all the $S/N > 5$ stacks from 2 to $4 \mu\text{m}$ and beyond, up to 30.1 ± 0.3 mag for the first (reddest) stack (including F480M+F444W), which reaches $\sim 5 \mu\text{m}$. For the SW stacks, no significant signal is recovered in any of them. We measure a 5σ upper limit of 31.0 mag for the stack adding all SW data. This implies an ~ 0.7 mag color jump from the NIRCam SW to the LW ranges.

The SED of *Cerberus* shown in Figure 5 is, in fact, very similar to the little red dots (LRDs) recently presented and characterized in a number of papers (e.g., Labb   et al. 2023a,b, Matthee et al. 2023, Barro et al. 2023, Williams et al. 2023a, P  rez-Gonz  lez et al. 2024, Kokorev et al. 2024), but shifted to longer wavelengths. The $F277W - F444W > 1$ mag general selection criterion of LRDs, and, more specifically, the 3 mag color of the example source 203749 in P  rez-Gonz  lez et al. (2024), compares well, if we multiply the observed wavelengths by a factor of ~ 2 , with the $F444W - F1000W \sim 3.5$ mag (or, using the F560W 5σ upper limit, $F560W - F1000W \gtrsim 2$ mag). The flat $F150W - F200W$ color distinctive of LRDs (the largest value allowed by the selection is typically 0.5 mag), i.e., a change in slope at around 0.3–0.4 μm in the rest-frame for the typical redshift of LRDs $5 < z < 9$, compares well with the color between 3 and 4 μm for *Cerberus*,

just multiplying again the observed wavelengths by a factor of ~ 2 . That rest-frame UV color is indeed consistent with the reddest LRDs in P  rez-Gonz  lez et al. (2024) or the LRD of which a NIRSpec spectrum was presented in Killi et al. (2023). The analogy can also be established in terms of the apparent magnitude: the typical magnitude of LRDs in the blue part of their SED lies around 27–28 mag, *Cerberus* being $\gtrsim 10$ times dimmer in NIRCam LW bands. We note that the difference in luminosity distance and cosmological dimming between $z \sim 7$, the median redshift of LRDs (P  rez-Gonz  lez et al. 2024) and $z \sim 14$ (a factor of 2 larger, see also Section 4.2.3) will translate to a flux ratio around an order of magnitude for the same type of object.

4.2. Analysis of the SED of *Cerberus*

In the following subsections, we discuss possible interpretations of the SED of *Cerberus*. The NIRCam and MIRI source (Figure 3) were observed more than one year apart. However, given the spatial coincidence of the object in the NIRCam and MIRI observations (centroids separated by $0''.016$), we proceed by assuming that they are the same object and not a chance alignment of two different objects.

4.2.1. Solar System origin

A bright mid-infrared object such as *Cerberus* matches the expected properties of Solar System bodies, e.g., asteroids. Given the long observational MIRI/F1000W campaign, we would expect to see proper motion, which is not the case, unless the asteroid is distant and/or near aphelion. However, the fact that the NIRCam data detect *Cerberus* (in stacked images) and the observations from MIDIS and JADES were taken more than one year apart indicates that *Cerberus* cannot be a Solar System body (assuming that the NIRCam and MIRI sources are the same object and not a fortuitous superposition). In Section 3.2, we also measure the centroid shift of the object between the MIRI and NIRCam data to $0''.016$ which is consistent with a zero offset. This makes the source even more unlikely to be a Solar System body.

4.2.2. Galactic origin

As shown by Langeroodi & Hjorth (2023a) and Hainline et al. (2023) for LRDs, red sources detected by JWST in cosmological fields such as GOODS-S can be brown dwarfs. Following the method in Langeroodi & Hjorth (2023a), we fit the photometry of *Cerberus* with brown dwarf atmosphere templates. We include the Sonora cloud-free models (Karalidi et al. 2021; Marley et al. 2021) as well as the ATMO2020++ cloud-free adiabat-adjusted T and Y dwarf models (Leggett et al. 2021; Meisner et al. 2023, see also Su  rez & Metchev

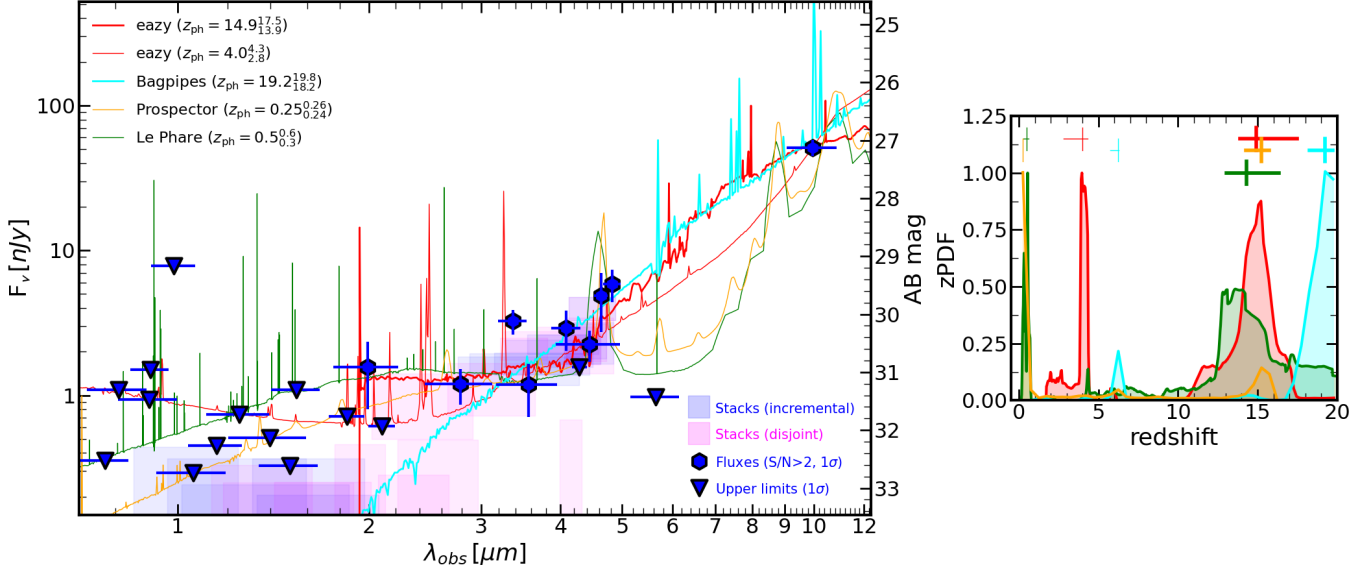


Figure 5. *Left:* Spectral energy distribution of *Cerberus*. Dots show flux measurements with $S/N > 2$ for individual NIRCam and MIRI bands (filter widths shown as horizontal bars), triangles depict 1σ upper limits. Shaded regions stand for flux measurements and filter widths for NIRCam stacks in the LW (actual $S/N > 5$ measurements in most stacks) and SW (upper limits in all of them) channels. Two sets of NIRCam stacks are considered: two incremental stacks starting from the red and blue ends, respectively, and stopping at $\sim 2 \mu\text{m}$; and 4 disjoint stacks, combining filters in groups of 2, 3, 4, and 5, with no filter in common between each set. The spectral energy distribution has been fitted with a battery of codes to estimate a photometric redshift. Most probable values and uncertainties are provided in the figure (for EAZY we provide 2 solutions since their peak probabilities are very similar), with low- z solutions plotted as thin lines, and high- z models as thick lines. *Right:* Photometric redshift probability distribution function for the modeling shown in the left panel. All distributions are normalized to unity at the peak. We show the main solutions, including all values provided in the spectral energy distribution plot and also secondary solutions at $z < 10$ and $z > 10$.

2022). In particular the ATMO2020++ models were included to ensure coverage of extremely cool brown dwarfs with $250 \text{ K} < T_{\text{eff}} < 500 \text{ K}$. Compared to warmer brown dwarfs, these models more closely resemble the SED shape of *Cerberus*, which is relatively faint at near-infrared wavelengths while getting significantly brighter at $10 \mu\text{m}$.

The best-fit brown dwarf template is shown in the top-left panel of Figure 6. We infer a best-fit effective temperature (T_{eff} [K]) of 300_{-25}^{+100} , surface gravity ($\log g$ [cm s^{-2}]) of $3.0_{-0.5}^{+1.0}$, and distance of 332 ± 67 pc. Its effective temperature would most likely classify *Cerberus* as a Y-type dwarf (see Figure 12 in Langeroodi & Hjorth 2023a). Compared to the UltracoolSheet compilation of known brown dwarfs with parallax distances (Best et al. 2020), its inferred distance (~ 300 pc) would make *Cerberus* one of the farthest (top 20) brown dwarfs discovered to date (see Figure 11 in Langeroodi & Hjorth 2023a). This distance at the high Galactic latitude of *Cerberus* would place it at the edge of the thin disk (see Figure 6 in Hainline et al. 2023). Recently, three T-type dwarfs were discovered and spectroscopically confirmed with NIRSpec prism (Langeroodi & Hjorth 2023a; Burgress et al. 2023) at estimated distances between 0.7

and 4.8 kpc, all most likely outside the thin disk; among them A2744-BD3 is a late T-type at 755 pc.

Our best-fit to a brown dwarf spectral template, shown in the top-left panel of Figure 6, nicely fit the F444W–F1000W color and is consistent with the non-detection in the deep MIDIS F560W data. However, that brown dwarf model is very red in both the NIRCam SW-to-LW and 3-to-4 μm colors, which is not favored by our measurements (in stacked data), pointing to a flatter SED.

In addition, both the MIRI and stacked NIRCam images (see Section 3.2) shows the source to be slightly extended and asymmetrical as compared to the PSF. The two instruments, NIRCam and MIRI, indicate a morphology for the source that makes it unlikely that it is a point source, thus disfavoring the *single* brown dwarf scenario. The slight extension of order $0''.1$ alone would however not argue against a brown dwarf *binary*. Even at only 100 pc distance, a semi-major axis of $0''.1$ for a binary of two identical brown dwarfs/planets with masses of $(0.0003 - 0.07) M_{\odot}$ each would result in orbit periods of order 100–1000 years, i.e., the elongated image would not vary between the NIRCam and the MIRI observations.

4.2.3. Extragalactic origin

The SED of *Cerberus* was fitted to estimate a photometric redshift and obtain its physical properties in a 2-step procedure. We used several codes for this purpose, separating the two tasks to analyze facets of each method and understand the (possibly systematic) uncertainties in detail. We used the fluxes plotted in Figure 5 as well as the ALMA upper limits quoted in Section 2, shown to be important for high redshift sources (even for determining their redshift, see Meyer et al. 2024), and particularly for an ERO such as *Cerberus*. The results are shown in Figures 6 and 7.

We first used the EAZY code (Brammer et al. 2008) to fit the data in 2 ways: one using actual (low S/N) flux measurements for all filters, and another replacing all $S/N < 3$ measurements by 5σ upper limits that templates were not allowed to surpass (achieved with a modified version of the code). We employed in the fits all v1.3 templates, which include a dusty galaxy with a high-equivalent width emission-line spectrum, as well as new models for little red dots and high-redshift AGN+torus recently added based on JWST data (Killi et al. 2023). We did not impose any prior and worked with minimum χ^2 photometric redshift estimates in the range $0 < z < 20$.

We also ran BAGPIPES (Carnall et al. 2018). BAGPIPES is a stellar population synthesis modeling package built on the updated Bruzual & Charlot (2003) spectral library with the 2016 version of the MILES library (Falcón-Barroso et al. 2011). It uses a Kroupa (2001) IMF. We adopted a Calzetti et al. (2000) dust attenuation allowing $0 < A_V < 8$ mag, and included nebular emission lines. The SFH is set to delayed- τ model and the code included an AGN component as in Carnall et al. (2023).

We fitted the extracted photometry of *Cerberus* with PROSPECTOR (Johnson et al. 2021) to constrain its photometric redshift and stellar population properties. We adopted the PROSPECTOR setup described in detail in Langeroodi et al. (2023) and Langeroodi & Hjorth (2023b). In brief, the SFH is modelled non-parametrically in five temporal bins with a continuity prior (see e.g., Leja et al. 2019); nebular emission is added from the CLOUDY (Chatzikos et al. 2023) runs compiled in Byler et al. (2017); we treat the nebular- and stellar- metallicity as independent free parameters; dust attenuation is modelled with a two-component model, one for the entire galaxy and one for the star-forming regions (Kriek & Conroy 2013). In a first PROSPECTOR run, redshift is fitted as a free parameter with a flat prior in $0 < z < 20$. We then re-ran the same PROSPECTOR setup, fixing the redshift to the best-fit values mutually

agreed using results from all the SED-fitting codes used in this work (see below).

Complementarily, we made use of LEPHARE++, the C++ latest evolution of the SED-fitting code LEPHARE (Arnouts et al. 2002; Ilbert et al. 2006) to fit the *Cerberus* photometry, following the approach of Moutard et al. (2024, in prep.). In brief, we considered stellar population synthesis models from Bruzual & Charlot (2003) with a Chabrier (2003) IMF and two metallicities (Z_\odot , $0.5 Z_\odot$), assuming exponential SFHs with $0.1 \leq \tau \leq 30$ Gyr, and delayed SFHs peaking after 1 and 3 Gyrs. To take into account the strong contribution from the nebular emission lines that can occur at very young ages, they are added following the line ratios adopted by Saito et al. (2020) and their normalization is allowed to vary by a factor of four. Aiming to take into account extremely dusty galaxies, attenuation is considered through the laws of Calzetti et al. (2000) and Arnouts et al. (2013), with $0 \leq E(B-V) \leq 1.5$ mag, and dust IR reemission is taken into account following Béthermin et al. (2012). We finally ran LEPHARE++ on a grid between redshift $z = 0$ and 20.

Apart from the previous codes, which were used to both constrain a photometric redshift and determine the physical properties of *Cerberus*, we also performed SED modeling with SYNTHESIZER-AGN and CIGALE, first fixing the redshift (to several values, see below).

The SYNTHESIZER-AGN code assumes that the SED can be modeled with a composite stellar population (Pérez-González et al. 2003, 2008) and AGN emission coming from the accretion disk and the dust torus (Pérez-González et al. 2024). The stellar emission includes a young and a more evolved star formation event, each one described by a delayed exponential function with timescales between 1 Myr and 1 Gyr, and with ages from 1 Myr up to the age of the Universe at the redshift of the source. The attenuations of the emission from each stellar population are independent and described by a Calzetti et al. (2000) law, with A_V values ranging from 0 to 10 mag for each population. The stellar emission is described by the Bruzual & Charlot (2003) models, assuming a Chabrier (2003) IMF with stellar mass limits between 0.1 and $100 M_\odot$, and the nebular emission is also considered (Pérez-González et al. 2003). The AGN emission is modeled with a QSO average spectrum (Vanden Berk et al. 2001; Glikman et al. 2006). The dust emission from the AGN is modeled with the self-consistent templates of AGN tori presented in Siebenmorgen et al. (2015), and dust emission linked to star formation is added using the models from Draine & Li (2007).

CIGALE (Boquien et al. 2019) SED-fitting analysis assume an SFH modelled using a constant star-formation rate with ages ranging from 1 to 100 Myr. We adopted the stellar populations models from Bruzual & Charlot (2003) with solar metallicity, and the Chabrier (2003) IMF. We included nebular continuum and emission lines using solar metallicity, electron density of 100 cm^{-3} , and ionised parameter equal to $\log(U) = -2$. The dust attenuation and far-IR emission uses the Calzetti Law (Calzetti et al. 2000) and the Draine et al. (2014) models, respectively. AGN emission is added using the Fritz et al. (2006) models following the initial parameters suggested by Ciesla et al. (2015).

The results of our photometric redshift analysis are given in Figure 5. All codes provide 2 main solutions and a number of tertiary redshift values. We mark the 2 main solutions at $z < 10$ and $z > 10$ for each code in the right panel of the figure. The obtained solutions are: $z \sim 0.4$ (provided by PROSPECTOR and LEPHARE++), $z \sim 4$ (very prominent solution for by EAZY, also detected weakly by PROSPECTOR and LEPHARE++), $z = 14 - 15$ (obtained by all codes), $z \sim 17$ (obtained by LEPHARE++), and $z \sim 19$ (obtained by BAGPIPES and LEPHARE++). We note that the $z \sim 0.4$ solution corresponds to a PAH line entering the F1000W passband, the $z \sim 4$ solution would imply $\text{Pa}\alpha$ covered by the filter, for $z \sim 15$, $\text{H}\alpha$ would contribute to the MIRI-F1000W flux, and $z \sim 19$ means that the F1000W emission could be enhanced by $\text{H}\beta$ and/or $[\text{O III}]\lambda\lambda 4960, 5008$ emission.

After identifying all possible solutions, we fixed the redshifts to the peaks showing the highest probabilities, namely $z = 0.4$, $z = 4$, and $z = 15$, and ran all codes to understand the implications on the nature of *Cerberus*. We analyze in detail the different possibilities to explain the SED of *Cerberus* in the following subsections. We provide best-fitting models in Figures 6 (focused on the spectral range typically dominated by stellar emission) and 7 (extending the SED plots to the spectral region that might be dominated by dust emission). The results are summarized in Table 1.

High- z solution: $z \sim 15$

All codes provide a photometric redshift solution around $z = 14 - 15$. As mentioned before, this solution would correspond to $\text{H}\alpha$ entering the F1000W filter, which would leave $\text{H}\beta$ and $[\text{O III}]\lambda\lambda 4960, 5008$ within the F770W filter.

In the absence of dust, the F444W–F1000W color is very difficult to reproduce with stars alone, even for the youngest and lowest metallicity models. Taking into account the width of the F1000W filter, even a $\text{H}\alpha$ line

with a prominent $EW = 3000\text{ \AA}$ (the limit for Starburst 99 models, Leitherer et al. 2002, using the lowest metallicities, the youngest ages, and setting all relevant parameters to their extreme values, e.g., ionizing photon escape fraction) would produce a relatively small flux density enhancement in the F1000W filter (around 1 mag). The only way to fit the full SED is including some red component, either a dusty starburst or an obscured AGN.

Indeed, the best fits for this $z \sim 15$ solution are obtained with two different models. The first possibility is a relatively dusty ($A_V > 1$ mag for all codes except PROSPECTOR, but we remark that this software internally increases the attenuation for younger stars), massive ($\sim 10^9\text{ M}_\odot$), and intermediate age (50–100 Myr mass-weighted age) starburst. Those numbers would translate to SFRs around $0.1 - 30\text{ M}_\odot\text{ yr}^{-1}$.

The second possibility is a model where a significant fraction of the F1000W flux comes from the emission from a dust torus, and there is some contribution to the SED coming from star formation, increasing towards the ultraviolet range. This solution allows a significantly smaller stellar mass, $\sim 10^7\text{ M}_\odot$, for SYNTHESIZER-AGN (with large uncertainties due to the overshining effect of the AGN) in a young (1 Myr age, $20\text{ M}_\odot\text{ yr}^{-1}$, $A_V \sim 0.2$ mag) star-forming galaxy. The other codes including an AGN, BAGPIPES and CIGALE, provide similar results, although the stellar attenuation is significantly higher, and the fits present problems in reproducing the ALMA upper limits (see Figure 7).

The obscured AGN fit to *Cerberus* SED resembles the results for the reddest LRDs at $5 < z < 9$, but within a $\gtrsim 100$ times less massive galaxy and at a 500(250) Myr earlier epoch compared to the average (maximum) redshift of LRDs (Pérez-González et al. 2024; Greene et al. 2023; Killi et al. 2023).

The derived bolometric luminosity of *Cerberus* for the $z = 15$ SYNTHESIZER-AGN solution is $10^{44.6 \pm 1.0}\text{ erg s}^{-1}$. Given the high redshift, the very red NIRCam-to-MIRI color, and the ALMA constraints, the torus models favored by this SED-fitting code peak at very short wavelengths ($\sim 20\text{ \mu m}$ rest-frame, $\sim 300\text{ \mu m}$ observed), as is shown in Figure 7. Translating those extreme conditions to a near- or even above-Eddington limit accretion, we could estimate the presence of a $\sim 10^{6.5 \pm 1.2}\text{ M}_\odot$ SMBH using the results in Woo & Urry (2002). We remark that these are very uncertain calculations because they are based on the F444W–F1000W measured color probing the bluest emission of the possibly present torus and the ALMA upper limits which probe the Rayleigh-Jeans tail of the torus emission. We should also consider that variations of the amount of stellar and nebular emis-

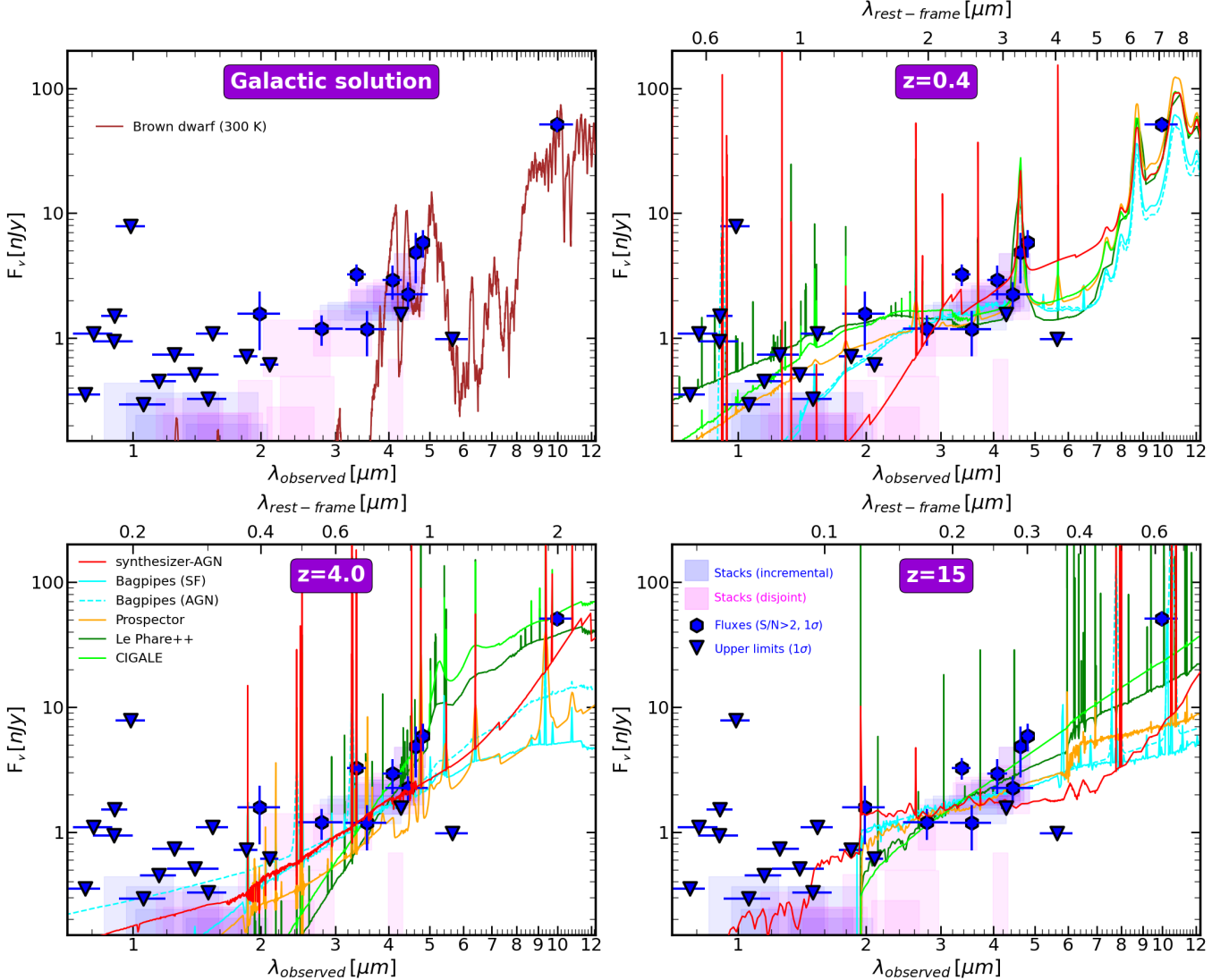


Figure 6. Detailed analysis of the spectral energy distribution of *Cerberus* for the main redshift solutions. The symbols are the same as described in Figure 5. We provide best-fitting models provided by different codes that include both stellar and AGN emission. The top-left panel shows the best-fitting brown dwarf template from the ATMO2020++ models, for a Y-type dwarf with an effective temperature of ~ 300 K at a distance of ~ 300 pc. The rest of the panels show results for $z = 0.4$ (top-right), $z = 3.5$ (bottom-left), and $z = 15$ (bottom-right). Main physical properties inferred with the modeling of the spectral energy distributions assuming an extragalactic origin are provided in Table 1.

sion strongly affect the bolometric luminosity calculation. Taking all the numbers above, and considering the mentioned caveats, the stellar to SMBH mass ratio would be around 0.2, consistent with the values discussed in Pacucci et al. (2023); Pacucci & Loeb (2024, see also Maiolino et al. 2023) for high redshift AGN discovered with JWST.

Intermediate- z solution: $z \sim 4$

A solution at $z \sim 4.0 \pm 0.3$ is the main one provided by EAZY, which could correspond to Pa α entering the F1000W passband (for $z > 3.8$). However, the best

EAZY template corresponds to a dusty galaxy (again, the NIRCam-MIRI color is too large for any other model). The dusty nature is confirmed by the more detailed SED modeling performed with SYNTHESIZER-AGN after fixing the redshift, which reproduces the SED with a $200 \text{ M}_\odot \text{ yr}^{-1}$, $A_V \sim 4$ mag, 5 Myr old starburst in a 10^8 M_\odot galaxy. BAGPIPES obtains very different solutions for the AGN and SF versions: a starburst (10 Myr old galaxy) 10^7 M_\odot galaxy with large amounts of dust, $A_V \sim 3$ mag, or an obscured AGN in a more massive post-starburst galaxy, $\sim 10^8 \text{ M}_\odot$, with older age and larger dust content. Similar properties are obtained with

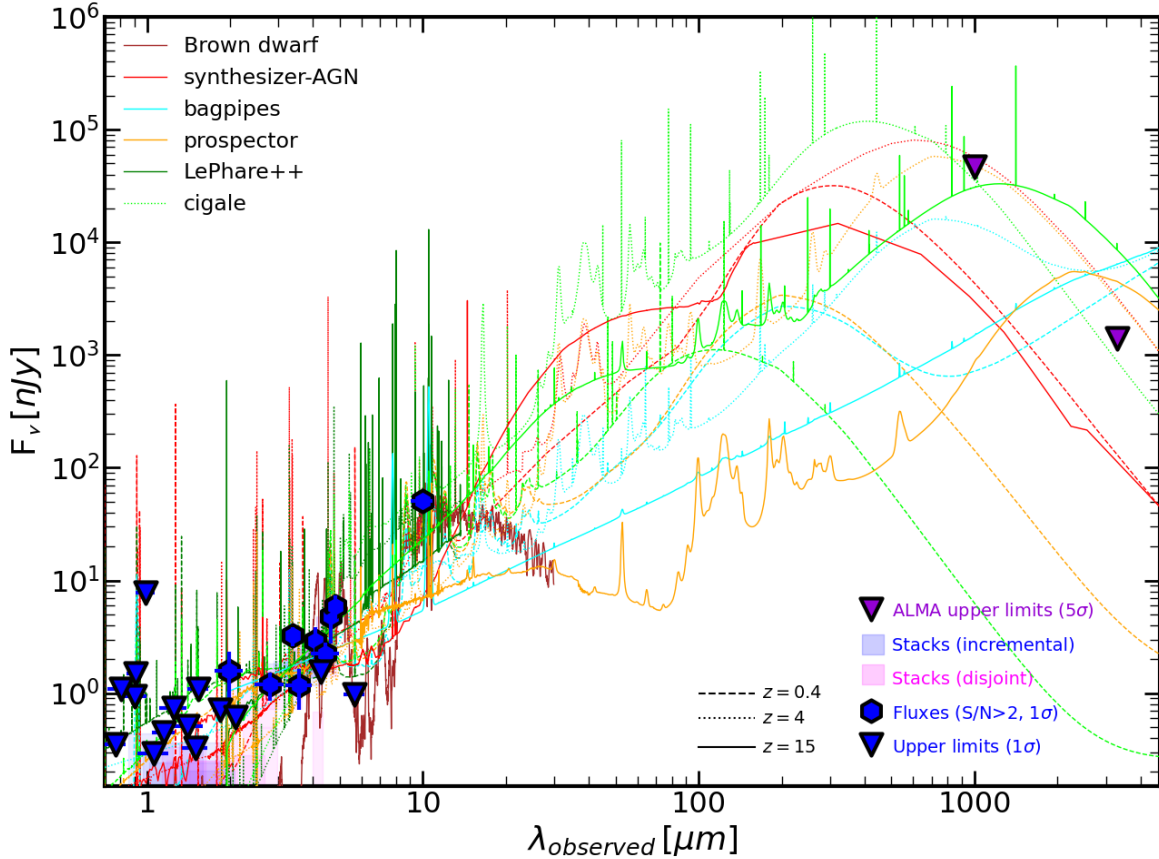


Figure 7. SED modeling results including the ALMA upper limits at 1.1 and 3.0 mm. Color code for data points and stacked data measurements is the same as in Figure 6. The modeling solutions at $z = 0.4$, $z = 4$, and $z = 15$ are shown with different line styles.

other codes, pointing to a dusty galaxy with a stellar mass one order of magnitude smaller than other analog sources discovered and/or analyzed with JWST (consistent with their brightest NIRCam magnitudes, see, e.g., Barrufet et al. 2023, Pérez-González et al. 2023a, or Williams et al. 2023a).

Within this redshift range, we should consider the possibility of *Cerberus* being an exotic type of faint, heavily obscured AGN whose SED differs substantially from the bright quasar templates included in our fitting codes (although it could be recovered with a QSO+torus composite by SYNTHESIZER-AGN). In particular, Hamann et al. (2017) report 5 – 10 ERQs at $2 < z < 3.5$ whose flux decrement between $12 \mu\text{m}$ and $1 \mu\text{m}$ is consistent with *Cerberus*. ERQs are characterized by faint and intrinsically red optical continua and abnormally strong emission lines and infrared emission; their SEDs are not part of standard AGN fitting libraries due to extreme rarity. However, all reported ERQs are brighter than

Cerberus by ~ 14 magnitudes. The AGN processes leading to ERQs are unknown, as is whether they can be sustained at much lower bolometric luminosities. Therefore, this possibility cannot be assessed quantitatively.

We note here that *Cerberus* is located very near ($\lesssim 1''$) 2 Lyman Alpha Emitters at $z = 4 - 5$, as presented in Bacon et al. (2023): ID7666 at $z_{\text{sp}} = 4.14$, and ID53 at $z_{\text{sp}} \simeq 4.77$. Besides, considering all the sources found in the MXDF between $3 \leq z < 5$ reported in Bacon et al. (2023) with reliable spectroscopic redshifts, our target lies in an overdense region of Lyman Alpha Emitters within a radius of 15 arcsec (i.e. about 100 pkpc). Within the 15 arcsec radius aperture, we find 17 galaxies between $3 \leq z < 3.5$, 10 galaxies at $3.5 \leq z < 4$, 5 objects at $4 \leq z < 4.5$ and 20 galaxies at $4.5 \leq z < 5$. This points to a somewhat similar case as the galaxy claimed to lie at $z \sim 16$ in the CEERS field (Donnan et al. 2023; Finkelstein et al. 2023; although other photometric redshift estimations provided $z \sim 5$, Pérez-González et al.

2023a) but being part of a large scale structure (Naidu et al. 2022, see also Zavala et al. 2023 for a discussion about dusty galaxies with $z < 5$ and $z > 10$ photometric redshift solutions) and finally confirmed to be at $z \sim 4.5$ (Arrabal Haro et al. 2023). Several cases like this one have been reported recently (Caputi et al. 2021; Kokorev et al. 2023).

Low- z solution: $z \sim 0.4$

For the last photometric redshift solution, $z < 0.5$, in this case provided by PROSPECTOR and LEPHARE++, we fixed the value for detailed SED modelling at $z \sim 0.4$. The F1000W flux here is dominated by the $7 \mu\text{m}$ PAH feature. This solution then implies a highly attenuated ($A_V \gtrsim 2$ mag) dwarf galaxy for all codes with a stellar mass $\sim 10^{5-6} M_\odot$. Alternatively, BAGPIPES-AGN reproduces the SED with an obscured AGN in a galaxy with a similar (small) stellar mass. The very small stellar mass, relatively high dust attenuation, and strong PAH emission is an uncommon combination, at odds with the mass-metallicity relationship (e.g., Tremonti et al. 2004) and the weakening of PAH features at low metallicities (e.g., Engelbracht et al. 2005).

4.2.4. Transient nature

The bright nature of *Cerberus* hints at a possible transient nature of the source. In fact, analyzing the 11 individual MIRI exposures (taken within a 10 hours window), and partial mosaics of the full dataset, we found that excluding 2 exposures from the stack implied that the source becomes 0.3–0.4 mag dimmer. The origin of this difference was linked to 2 contiguous exposures, numbers 7 and 8. This is a small difference (within 2σ of the quoted F1000W magnitude), but the fact that the 2 exposures are contiguous might be linked to the source having a transient nature. Alternatively, it might have originated from some transient effect on the detector, for example, cosmic ray showers (although no hit was detected by the pipeline). If the origin is astrophysical, it could be explained in terms of variability of a rotating asteroid (Sanchez et al. 2017, although we do not detect any proper motion within a year, see Section 4.2.1), a brown dwarf (e.g., Artigau et al. 2009), or an AGN (Sheng et al. 2017).

5. SUMMARY AND CONCLUSIONS

We report the discovery of a NIRCam-dark source identified in the MIRI Deep Imaging Survey (MIDIS) of the Hubble Ultra Deep Field carried out with the F1000W filter. We call this source *Cerberus*. The source has a magnitude around 27 mag (6σ) in F1000W and is extremely faint in all the NIRCam data taken by the

deepest survey on the sky, the JWST Advanced Deep Extragalactic Survey, JADES, implying a magnitude fainter than ~ 30.5 at wavelengths $\lesssim 5 \mu\text{m}$. *Cerberus* is also undetected in the MIDIS F560W ultra-deep observations of the field, i.e., $F560W \gtrsim 29$ mag. Our analysis of MIRI F1000W mosaics produced with limited datasets as well as the detection in NIRCam stacks at $\sim 5\sigma$ level at wavelengths longer than $\sim 3 \mu\text{m}$, both confirm *Cerberus* is real and qualifies as an extremely red object, with a color around $F444W-F1000W \sim 3.5$ mag and $F560W-F1000W \gtrsim 2$ mag. The morphology of the source in the MIRI F1000W image matches that observed in the NIRCam stacked data (with 1 year passing between both observations), in both cases presenting a main point-like component and similar-sized (i.e., unresolved) haze, further supporting that *Cerberus* is a real source not linked to a fortuitous alignment.

We discuss the possible nature of *Cerberus* and identify 2 possible Galactic source types and 3 different kinds of galaxy that could match its spectral energy distribution.

Given that the MIRI and NIRCam observations were taken with a one year epoch difference, we discard a Solar System origin. The NIRCam-to-NIRCam and NIRCam-to-MIRI colors do not match any known substellar object, even the coolest and reddest brown dwarfs present mid-infrared colors that are not compatible with the spectral energy distribution of *Cerberus*.

Concerning an extragalactic origin, we identify 3 possibilities:

- A low-redshift solution, $z \sim 0.4$, would imply that *Cerberus* is a dusty galaxy with strong emission from polycyclic aromatic hydrocarbons or warm dust heated by an active galactic nucleus. The low mass obtained for this solution, $M_\star \sim 10^5 M_\odot$, would point to an unknown type of dwarf galaxy with large dust content and no PAH depletion.
- The second possibility is a dusty starburst or post-starburst galaxy, or a galaxy hosting a mid-infrared bright obscured active galactic nucleus, at $z \sim 4$ with a stellar mass $M \sim 10^8 M_\odot$ and around $A_V > 2$ mag of extinction.
- The third possibility is a $z \sim 15$ galaxy, the colors of which could be understood if we assume its spectral energy distribution is dominated by an obscured active nucleus with a bright torus significantly contributing to the flux in the rest-frame optical range, and the super-massive black hole to stellar mass ratio is around 0.2. This fit would leave room for some additional contribution from stellar emission, perhaps dominating the

rest-frame ultraviolet, and providing a stellar mass around $M_\star \sim 10^7 M_\odot$. The latter number is, however, very uncertain due to the overshining effect of the torus. Alternatively, the spectral energy distribution can be reproduced with a relatively massive ($M_\star \sim 10^9 M_\odot$) dusty ($A_V > 1$ mag) galaxy.

Despite vetting all the imaging data meticulously, confirming beyond doubt that the source is real, we have to accept that the available data are insufficient to establish the true nature of *Cerberus* with certainty. Given that the source is located in the deepest HST and JWST field, deeper imaging will likely be available in the near future and help to obtain a better understanding of this unique object. In any case, further investigation of *Cerberus* will challenge the capabilities of JWST, as it was the case in the past for objects discovered at the limit of photometric surveys (remarkably, with space-based missions such as HST or *Spitzer*), whose spectroscopic follow-up (typically with ground-based facilities) was tremendously exigent (but still attempted with varying success). The discovery and analysis presented in this letter demonstrates the feasibility of identifying NIRCam-dark sources when selected as extremely red objects with MIRI observations up to at least $10 \mu\text{m}$, maybe revealing new types of Milky Way sub-stellar bodies or of galaxy populations more easily detectable through ultra-deep photometric surveys in (some of) the reddest wavelengths probed by JWST.

REFERENCES

Alcalde Pampliega, B., Pérez-González, P. G., Barro, G., et al. 2019, *ApJ*, 876, 135, doi: [10.3847/1538-4357/ab14f2](https://doi.org/10.3847/1538-4357/ab14f2)

Arnouts, S., Moscardini, L., Vanzella, E., et al. 2002, *MNRAS*, 329, 355, doi: [10.1046/j.1365-8711.2002.04988.x](https://doi.org/10.1046/j.1365-8711.2002.04988.x)

1 PGP-G and LC acknowledge support from
 2 grant PID2022-139567NB-I00 funded by Span-
 3 ish Ministerio de Ciencia e Innovación
 4 MCIN/AEI/10.13039/501100011033, FEDER *Una*
 5 *manera de hacer Europa*. KIC and EI acknowledge
 6 funding from the Netherlands Research School for As-
 7 tronomy (NOVA). KIC acknowledges funding from the
 8 Dutch Research Council (NWO) through the award
 9 of the Vici Grant VI.C.212.036. MA acknowledges
 10 financial support from Comunidad de Madrid under
 11 Atracción de Talento grant 2020-T2/TIC-19971. DL
 12 and JH were supported by a VILLUM FONDEN Inves-
 13 tigator grant (project number 16599). This work was
 14 supported by a research grant (VIL54489) from VIL-
 15 LUM FONDEN. SG acknowledges financial support
 16 from the Villum Young Investigator grant 37440 and
 17 13160 and the Cosmic Dawn Center (DAWN), funded
 18 by the Danish National Research Foundation (DNRF)
 19 under grant No. 140. JPP acknowledges financial sup-
 20 port from the UK Science and Technology Facilities
 21 Council, and the UK Space Agency. TPR acknowledges
 22 support from ERC Advanced Grant 743029 EASY.
 23 AAH acknowledges support from grant PID2021-
 24 124665NB-I00 funded by the Spanish Ministry of Sci-
 25 ence and Innovation and the State Agency of Research
 26 MCIN/AEI/10.13039/501100011033 and ERDF A way
 27 of making Europe. JA-M, AC-G, LC acknowledge sup-
 28 port by grant PIB2021-127718NB-100 from the Spanish
 29 Ministry of Science and Innovation/State Agency of
 30 Research MCIN/AEI/10.13039/501100011033 and by
 31 “ERDF A way of making Europe”. SEIB is funded
 32 by the Deutsche Forschungsgemeinschaft (DFG) un-
 33 der Emmy Noether grant number BO 5771/1-1. JM,
 34 GÖ and AB acknowledge support from the Swedish
 35 National Space Administration (SNSA). RAM acknowl-
 36 edges support from the Swiss National Science Founda-
 37 tion (SNSF) through project grant 200020.207349.

38 Some of the data presented in this paper were ob-
 39 tained from the Mikulski Archive for Space Telescopes
 40 (MAST) at the Space Telescope Science Institute. The
 41 specific observations analyzed can be accessed via DOI:
 42 [10.17909/je9x-d314](https://doi.org/10.17909/je9x-d314) DOI: [10.17909/je9x-d314](https://doi.org/10.17909/je9x-d314).

Arnouts, S., Le Floc'h, E., Chevallard, J., et al. 2013, *A&A*, 558, A67, doi: [10.1051/0004-6361/201321768](https://doi.org/10.1051/0004-6361/201321768)

Arrabal Haro, P., Dickinson, M., Finkelstein, S. L., et al. 2023, *Nature*, 622, 707, doi: [10.1038/s41586-023-06521-7](https://doi.org/10.1038/s41586-023-06521-7)

Artigau, É., Bouchard, S., Doyon, R., & Lafrenière, D. 2009, *ApJ*, 701, 1534, doi: [10.1088/0004-637X/701/2/1534](https://doi.org/10.1088/0004-637X/701/2/1534)

Bacon, R., Accardo, M., Adjali, L., et al. 2010, in Society of Photo-Optical Instrumentation Engineers (SPIE) Conference Series, Vol. 7735, Ground-based and Airborne Instrumentation for Astronomy III, ed. I. S. McLean, S. K. Ramsay, & H. Takami, 773508, doi: [10.1117/12.856027](https://doi.org/10.1117/12.856027)

Bacon, R., Conseil, S., Mary, D., et al. 2017, *A&A*, 608, A1, doi: [10.1051/0004-6361/201730833](https://doi.org/10.1051/0004-6361/201730833)

Bacon, R., Brinchmann, J., Conseil, S., et al. 2023, *A&A*, 670, A4, doi: [10.1051/0004-6361/202244187](https://doi.org/10.1051/0004-6361/202244187)

Bagley, M. B., Pirzkal, N., Finkelstein, S. L., et al. 2023, arXiv e-prints, arXiv:2302.05466, doi: [10.48550/arXiv.2302.05466](https://doi.org/10.48550/arXiv.2302.05466)

Barro, G., Perez-Gonzalez, P. G., Kocevski, D. D., et al. 2023, arXiv e-prints, arXiv:2305.14418, doi: [10.48550/arXiv.2305.14418](https://doi.org/10.48550/arXiv.2305.14418)

Barrufet, L., Oesch, P. A., Weibel, A., et al. 2023, *MNRAS*, 522, 449, doi: [10.1093/mnras/stad947](https://doi.org/10.1093/mnras/stad947)

Bertin, E., & Arnouts, S. 1996, *A&AS*, 117, 393, doi: [10.1051/aas:1996164](https://doi.org/10.1051/aas:1996164)

Best, W. M. J., Dupuy, T. J., Liu, M. C., Siverd, R. J., & Zhang, Z. 2020, The UltracoolSheet: Photometry, Astrometry, Spectroscopy, and Multiplicity for 3000+ Ultracool Dwarfs and Imaged Exoplanets, 1.0.1, Zenodo, doi: [10.5281/zenodo.4570814](https://doi.org/10.5281/zenodo.4570814)

Béthermin, M., Daddi, E., Magdis, G., et al. 2012, *ApJL*, 757, L23, doi: [10.1088/2041-8205/757/2/L23](https://doi.org/10.1088/2041-8205/757/2/L23)

Blain, A. W., Smail, I., Ivison, R. J., Kneib, J. P., & Frayer, D. T. 2002, *PhR*, 369, 111, doi: [10.1016/S0370-1573\(02\)00134-5](https://doi.org/10.1016/S0370-1573(02)00134-5)

Boquien, M., Burgarella, D., Roehlly, Y., et al. 2019, *A&A*, 622, A103, doi: [10.1051/0004-6361/201834156](https://doi.org/10.1051/0004-6361/201834156)

Bouwens, R. J., Illingworth, G. D., Oesch, P. A., et al. 2011, *ApJ*, 737, 90, doi: [10.1088/0004-637X/737/2/90](https://doi.org/10.1088/0004-637X/737/2/90)

Brammer, G. B., van Dokkum, P. G., & Coppi, P. 2008, *ApJ*, 686, 1503, doi: [10.1086/591786](https://doi.org/10.1086/591786)

Bruzual, G., & Charlot, S. 2003, *MNRAS*, 344, 1000, doi: [10.1046/j.1365-8711.2003.06897.x](https://doi.org/10.1046/j.1365-8711.2003.06897.x)

Burgasser, A. J., Gerasimov, R., Bezanson, R., et al. 2023, arXiv e-prints, arXiv:2308.12107, doi: [10.48550/arXiv.2308.12107](https://doi.org/10.48550/arXiv.2308.12107)

Byler, N., Dalcanton, J. J., Conroy, C., & Johnson, B. D. 2017, *ApJ*, 840, 44, doi: [10.3847/1538-4357/aa6c66](https://doi.org/10.3847/1538-4357/aa6c66)

Calzetti, D., Armus, L., Bohlin, R. C., et al. 2000, *ApJ*, 533, 682, doi: [10.1086/308692](https://doi.org/10.1086/308692)

Caputi, K. I., Lagache, G., Yan, L., et al. 2007, *ApJ*, 660, 97, doi: [10.1086/512667](https://doi.org/10.1086/512667)

Caputi, K. I., Caminha, G. B., Fujimoto, S., et al. 2021, *ApJ*, 908, 146, doi: [10.3847/1538-4357/abd4d0](https://doi.org/10.3847/1538-4357/abd4d0)

Carnall, A. C., McLure, R. J., Dunlop, J. S., & Davé, R. 2018, *MNRAS*, 480, 4379, doi: [10.1093/mnras/sty2169](https://doi.org/10.1093/mnras/sty2169)

Carnall, A. C., McLure, R. J., Dunlop, J. S., et al. 2023, *Nature*, 619, 716, doi: [10.1038/s41586-023-06158-6](https://doi.org/10.1038/s41586-023-06158-6)

Chabrier, G. 2003, *PASP*, 115, 763, doi: [10.1086/376392](https://doi.org/10.1086/376392)

Chapman, S. C., Blain, A. W., Smail, I., & Ivison, R. J. 2005, *ApJ*, 622, 772, doi: [10.1086/428082](https://doi.org/10.1086/428082)

Chatzikos, M., Bianchi, S., Camilloni, F., et al. 2023, *RMxAA*, 59, 327, doi: [10.22201/ia.01851101p.2023.59.02.12](https://doi.org/10.22201/ia.01851101p.2023.59.02.12)

Ciesla, L., Charmandaris, V., Georgakakis, A., et al. 2015, *A&A*, 576, A10, doi: [10.1051/0004-6361/201425252](https://doi.org/10.1051/0004-6361/201425252)

Decarli, R., Walter, F., Gómez-López, J., et al. 2019, *ApJ*, 882, 138, doi: [10.3847/1538-4357/ab30fe](https://doi.org/10.3847/1538-4357/ab30fe)

Decarli, R., Aravena, M., Boogaard, L., et al. 2020, *ApJ*, 902, 110, doi: [10.3847/1538-4357/abaa3b](https://doi.org/10.3847/1538-4357/abaa3b)

Dey, A., Soifer, B. T., Desai, V., et al. 2008, *ApJ*, 677, 943, doi: [10.1086/529516](https://doi.org/10.1086/529516)

Donnan, C. T., McLeod, D. J., Dunlop, J. S., et al. 2023, *MNRAS*, 518, 6011, doi: [10.1093/mnras/stac3472](https://doi.org/10.1093/mnras/stac3472)

Draine, B. T., & Li, A. 2007, *ApJ*, 657, 810, doi: [10.1086/511055](https://doi.org/10.1086/511055)

Draine, B. T., Aniano, G., Krause, O., et al. 2014, *ApJ*, 780, 172, doi: [10.1088/0004-637X/780/2/172](https://doi.org/10.1088/0004-637X/780/2/172)

Eisenstein, D. J., Willott, C., Alberts, S., et al. 2023a, arXiv e-prints, arXiv:2306.02465, doi: [10.48550/arXiv.2306.02465](https://doi.org/10.48550/arXiv.2306.02465)

Eisenstein, D. J., Johnson, B. D., Robertson, B., et al. 2023b, arXiv e-prints, arXiv:2310.12340, doi: [10.48550/arXiv.2310.12340](https://doi.org/10.48550/arXiv.2310.12340)

Elbaz, D., Cesarsky, C. J., Chanial, P., et al. 2002, *A&A*, 384, 848, doi: [10.1051/0004-6361:20020106](https://doi.org/10.1051/0004-6361:20020106)

Elston, R., Rieke, G. H., & Rieke, M. J. 1988, *ApJL*, 331, L77, doi: [10.1086/185239](https://doi.org/10.1086/185239)

Engelbracht, C. W., Gordon, K. D., Rieke, G. H., et al. 2005, *ApJL*, 628, L29, doi: [10.1086/432613](https://doi.org/10.1086/432613)

Falcón-Barroso, J., Sánchez-Blázquez, P., Vazdekis, A., et al. 2011, *A&A*, 532, A95, doi: [10.1051/0004-6361/201116842](https://doi.org/10.1051/0004-6361/201116842)

Finkelstein, S. L., Bagley, M. B., Ferguson, H. C., et al. 2023, *ApJL*, 946, L13, doi: [10.3847/2041-8213/acade4](https://doi.org/10.3847/2041-8213/acade4)

Franco, M., Elbaz, D., Béthermin, M., et al. 2018, *A&A*, 620, A152, doi: [10.1051/0004-6361/201832928](https://doi.org/10.1051/0004-6361/201832928)

Franx, M., Labbé, I., Rudnick, G., et al. 2003, *ApJL*, 587, L79, doi: [10.1086/375155](https://doi.org/10.1086/375155)

Fritz, J., Franceschini, A., & Hatziminaoglou, E. 2006, *MNRAS*, 366, 767, doi: [10.1111/j.1365-2966.2006.09866.x](https://doi.org/10.1111/j.1365-2966.2006.09866.x)

Galametz, A., Grazian, A., Fontana, A., et al. 2013, *ApJS*, 206, 10, doi: [10.1088/0067-0049/206/2/10](https://doi.org/10.1088/0067-0049/206/2/10)

Gillman, S., Gullberg, B., Brammer, G., et al. 2023, *A&A*, 676, A26, doi: [10.1051/0004-6361/202346531](https://doi.org/10.1051/0004-6361/202346531)

Glikman, E., Helfand, D. J., & White, R. L. 2006, *ApJ*, 640, 579, doi: [10.1086/500098](https://doi.org/10.1086/500098)

González-López, J., Decarli, R., Pavesi, R., et al. 2019, *ApJ*, 882, 139, doi: [10.3847/1538-4357/ab3105](https://doi.org/10.3847/1538-4357/ab3105)

González-López, J., Novak, M., Decarli, R., et al. 2020, *ApJ*, 897, 91, doi: [10.3847/1538-4357/ab765b](https://doi.org/10.3847/1538-4357/ab765b)

Graham, J. R., & Dey, A. 1996, *ApJ*, 471, 720, doi: [10.1086/178000](https://doi.org/10.1086/178000)

Greene, J. E., Labbé, I., Goulding, A. D., et al. 2023, arXiv e-prints, arXiv:2309.05714, doi: [10.48550/arXiv.2309.05714](https://doi.org/10.48550/arXiv.2309.05714)

Grogin, N. A., Kocevski, D. D., Faber, S. M., et al. 2011, *ApJS*, 197, 35, doi: [10.1088/0067-0049/197/2/35](https://doi.org/10.1088/0067-0049/197/2/35)

Hainline, K. N., Helton, J. M., Johnson, B. D., et al. 2023, arXiv e-prints, arXiv:2309.03250, doi: [10.48550/arXiv.2309.03250](https://doi.org/10.48550/arXiv.2309.03250)

Hamann, F., Zakamska, N. L., Ross, N., et al. 2017, *MNRAS*, 464, 3431, doi: [10.1093/mnras/stw2387](https://doi.org/10.1093/mnras/stw2387)

Hughes, D. H., Serjeant, S., Dunlop, J., et al. 1998, *Nature*, 394, 241, doi: [10.1038/28328](https://doi.org/10.1038/28328)

Ilbert, O., Arnouts, S., McCracken, H. J., et al. 2006, *A&A*, 457, 841, doi: [10.1051/0004-6361:20065138](https://doi.org/10.1051/0004-6361:20065138)

Johnson, B. D., Leja, J., Conroy, C., & Speagle, J. S. 2021, *ApJS*, 254, 22, doi: [10.3847/1538-4365/abef67](https://doi.org/10.3847/1538-4365/abef67)

Karalidi, T., Marley, M., Fortney, J. J., et al. 2021, *ApJ*, 923, 269, doi: [10.3847/1538-4357/ac3140](https://doi.org/10.3847/1538-4357/ac3140)

Killi, M., Watson, D., Brammer, G., et al. 2023, arXiv e-prints, arXiv:2312.03065, doi: [10.48550/arXiv.2312.03065](https://doi.org/10.48550/arXiv.2312.03065)

Kocevski, D. D., Onoue, M., Inayoshi, K., et al. 2023, *ApJL*, 954, L4, doi: [10.3847/2041-8213/ace5a0](https://doi.org/10.3847/2041-8213/ace5a0)

Koekemoer, A. M., Faber, S. M., Ferguson, H. C., et al. 2011, *ApJS*, 197, 36, doi: [10.1088/0067-0049/197/2/36](https://doi.org/10.1088/0067-0049/197/2/36)

Koekemoer, A. M., Ellis, R. S., McLure, R. J., et al. 2013, *ApJS*, 209, 3, doi: [10.1088/0067-0049/209/1/3](https://doi.org/10.1088/0067-0049/209/1/3)

Kokorev, V., Jin, S., Magdis, G. E., et al. 2023, *ApJL*, 945, L25, doi: [10.3847/2041-8213/acbd9d](https://doi.org/10.3847/2041-8213/acbd9d)

Kokorev, V., Caputi, K. I., Greene, J. E., et al. 2024, arXiv e-prints, arXiv:2401.09981, doi: [10.48550/arXiv.2401.09981](https://doi.org/10.48550/arXiv.2401.09981)

Kolb, J., Madec, P.-Y., Arsenault, R., et al. 2016, in Society of Photo-Optical Instrumentation Engineers (SPIE) Conference Series, Vol. 9909, Adaptive Optics Systems V, ed. E. Marchetti, L. M. Close, & J.-P. Véran, 99092S, doi: [10.1117/12.2232788](https://doi.org/10.1117/12.2232788)

Kriek, M., & Conroy, C. 2013, *ApJL*, 775, L16, doi: [10.1088/2041-8205/775/1/L16](https://doi.org/10.1088/2041-8205/775/1/L16)

Kroupa, P. 2001, *MNRAS*, 322, 231, doi: [10.1046/j.1365-8711.2001.04022.x](https://doi.org/10.1046/j.1365-8711.2001.04022.x)

Labbé, I., van Dokkum, P., Nelson, E., et al. 2023a, *Nature*, 616, 266, doi: [10.1038/s41586-023-05786-2](https://doi.org/10.1038/s41586-023-05786-2)

Labbé, I., Greene, J. E., Bezanson, R., et al. 2023b, arXiv e-prints, arXiv:2306.07320, doi: [10.48550/arXiv.2306.07320](https://doi.org/10.48550/arXiv.2306.07320)

Langeroodi, D., & Hjorth, J. 2023a, *ApJL*, 957, L27, doi: [10.3847/2041-8213/acfeec](https://doi.org/10.3847/2041-8213/acfeec)

—. 2023b, arXiv e-prints, arXiv:2307.06336, doi: [10.48550/arXiv.2307.06336](https://doi.org/10.48550/arXiv.2307.06336)

Langeroodi, D., Hjorth, J., Chen, W., et al. 2023, *ApJ*, 957, 39, doi: [10.3847/1538-4357/acdbc1](https://doi.org/10.3847/1538-4357/acdbc1)

Le Floc'h, E., Papovich, C., Dole, H., et al. 2005, *ApJ*, 632, 169, doi: [10.1086/432789](https://doi.org/10.1086/432789)

Leggett, S. K., Tremblin, P., Phillips, M. W., et al. 2021, *ApJ*, 918, 11, doi: [10.3847/1538-4357/ac0cfe](https://doi.org/10.3847/1538-4357/ac0cfe)

Leitherer, C., Li, I. H., Calzetti, D., & Heckman, T. M. 2002, *ApJS*, 140, 303, doi: [10.1086/342486](https://doi.org/10.1086/342486)

Leja, J., Carnall, A. C., Johnson, B. D., Conroy, C., & Speagle, J. S. 2019, *ApJ*, 876, 3, doi: [10.3847/1538-4357/ab133c](https://doi.org/10.3847/1538-4357/ab133c)

Madau, P., & Dickinson, M. 2014, *ARA&A*, 52, 415, doi: [10.1146/annurev-astro-081811-125615](https://doi.org/10.1146/annurev-astro-081811-125615)

Madec, P. Y., Arsenault, R., Kuntschner, H., et al. 2018, in Society of Photo-Optical Instrumentation Engineers (SPIE) Conference Series, Vol. 10703, Adaptive Optics Systems VI, ed. L. M. Close, L. Schreiber, & D. Schmidt, 1070302, doi: [10.1117/12.2312428](https://doi.org/10.1117/12.2312428)

Magnelli, B., Elbaz, D., Chary, R. R., et al. 2009, *A&A*, 496, 57, doi: [10.1051/0004-6361:200811443](https://doi.org/10.1051/0004-6361:200811443)

Maiolino, R., Scholtz, J., Curtis-Lake, E., et al. 2023, arXiv e-prints, arXiv:2308.01230, doi: [10.48550/arXiv.2308.01230](https://doi.org/10.48550/arXiv.2308.01230)

Marley, M. S., Saumon, D., Visscher, C., et al. 2021, *ApJ*, 920, 85, doi: [10.3847/1538-4357/ac141d](https://doi.org/10.3847/1538-4357/ac141d)

Matthee, J., Naidu, R. P., Brammer, G., et al. 2023, arXiv e-prints, arXiv:2306.05448, doi: [10.48550/arXiv.2306.05448](https://doi.org/10.48550/arXiv.2306.05448)

McCarthy, P. J. 2004, *ARA&A*, 42, 477, doi: [10.1146/annurev.astro.42.053102.134032](https://doi.org/10.1146/annurev.astro.42.053102.134032)

Meisner, A. M., Leggett, S. K., Logsdon, S. E., et al. 2023, *AJ*, 166, 57, doi: [10.3847/1538-3881/acdb68](https://doi.org/10.3847/1538-3881/acdb68)

Melinder, J., Östlin, G., Hayes, M., et al. 2023, *ApJS*, 266, 15, doi: [10.3847/1538-4365/acc2b8](https://doi.org/10.3847/1538-4365/acc2b8)

Meyer, R. A., Barrufet, L., Boogaard, L. A., et al. 2024, *A&A*, 681, L3, doi: [10.1051/0004-6361/202348306](https://doi.org/10.1051/0004-6361/202348306)

Naidu, R. P., Oesch, P. A., Setton, D. J., et al. 2022, arXiv e-prints, arXiv:2208.02794, doi: [10.48550/arXiv.2208.02794](https://doi.org/10.48550/arXiv.2208.02794)

Narayanan, D., Dey, A., Hayward, C. C., et al. 2010, MNRAS, 407, 1701, doi: [10.1111/j.1365-2966.2010.16997.x](https://doi.org/10.1111/j.1365-2966.2010.16997.x)

Oesch, P. A., Brammer, G., van Dokkum, P. G., et al. 2016, ApJ, 819, 129, doi: [10.3847/0004-637X/819/2/129](https://doi.org/10.3847/0004-637X/819/2/129)

Oesch, P. A., Brammer, G., Naidu, R. P., et al. 2023, MNRAS, 525, 2864, doi: [10.1093/mnras/stad2411](https://doi.org/10.1093/mnras/stad2411)

Oke, J. B., & Gunn, J. E. 1983, ApJ, 266, 713, doi: [10.1086/160817](https://doi.org/10.1086/160817)

Pacucci, F., & Loeb, A. 2024, arXiv e-prints, arXiv:2401.04159, doi: [10.48550/arXiv.2401.04159](https://doi.org/10.48550/arXiv.2401.04159)

Pacucci, F., Nguyen, B., Carniani, S., Maiolino, R., & Fan, X. 2023, ApJL, 957, L3, doi: [10.3847/2041-8213/ad0158](https://doi.org/10.3847/2041-8213/ad0158)

Papovich, C., Cole, J. W., Yang, G., et al. 2023, ApJL, 949, L18, doi: [10.3847/2041-8213/acc948](https://doi.org/10.3847/2041-8213/acc948)

Pérez-González, P. G., Gil de Paz, A., Zamorano, J., et al. 2003, MNRAS, 338, 508, doi: [10.1046/j.1365-8711.2003.06077.x](https://doi.org/10.1046/j.1365-8711.2003.06077.x)

Pérez-González, P. G., Rieke, G. H., Egami, E., et al. 2005, ApJ, 630, 82, doi: [10.1086/431894](https://doi.org/10.1086/431894)

Pérez-González, P. G., Rieke, G. H., Villar, V., et al. 2008, ApJ, 675, 234, doi: [10.1086/523690](https://doi.org/10.1086/523690)

Pérez-González, P. G., Barro, G., Annunziatella, M., et al. 2023a, ApJL, 946, L16, doi: [10.3847/2041-8213/acb3a5](https://doi.org/10.3847/2041-8213/acb3a5)

Pérez-González, P. G., Costantin, L., Langeroodi, D., et al. 2023b, ApJL, 951, L1, doi: [10.3847/2041-8213/acf9d0](https://doi.org/10.3847/2041-8213/acf9d0)

Pérez-González, P. G., Barro, G., Rieke, G. H., et al. 2024, arXiv e-prints, arXiv:2401.08782, doi: [10.48550/arXiv.2401.08782](https://doi.org/10.48550/arXiv.2401.08782)

Perrin, M. D., Sivarajamakrishnan, A., Lajoie, C.-P., et al. 2014, in Society of Photo-Optical Instrumentation Engineers (SPIE) Conference Series, Vol. 9143, Space Telescopes and Instrumentation 2014: Optical, Infrared, and Millimeter Wave, ed. J. Oschmann, Jacobus M., M. Clampin, G. G. Fazio, & H. A. MacEwen, 91433X, doi: [10.1117/12.2056689](https://doi.org/10.1117/12.2056689)

Pozzetti, L., & Mannucci, F. 2000, MNRAS, 317, L17, doi: [10.1046/j.1365-8711.2000.03829.x](https://doi.org/10.1046/j.1365-8711.2000.03829.x)

Rieke, G. H., Wright, G. S., Böker, T., et al. 2015, PASP, 127, 584, doi: [10.1086/682252](https://doi.org/10.1086/682252)

Rieke, M. J., Robertson, B., Tacchella, S., et al. 2023, ApJS, 269, 16, doi: [10.3847/1538-4365/acf44d](https://doi.org/10.3847/1538-4365/acf44d)

Rinaldi, P., Caputi, K. I., Costantin, L., et al. 2023, ApJ, 952, 143, doi: [10.3847/1538-4357/acdc27](https://doi.org/10.3847/1538-4357/acdc27)

Saito, S., de la Torre, S., Ilbert, O., et al. 2020, MNRAS, 494, 199, doi: [10.1093/mnras/staa727](https://doi.org/10.1093/mnras/staa727)

Sanchez, J. A., Reddy, V., Shepard, M. K., et al. 2017, AJ, 153, 29, doi: [10.3847/1538-3881/153/1/29](https://doi.org/10.3847/1538-3881/153/1/29)

Sanders, D. B., & Mirabel, I. F. 1996, ARA&A, 34, 749, doi: [10.1146/annurev.astro.34.1.749](https://doi.org/10.1146/annurev.astro.34.1.749)

Sheng, Z., Wang, T., Jiang, N., et al. 2017, ApJL, 846, L7, doi: [10.3847/2041-8213/aa85de](https://doi.org/10.3847/2041-8213/aa85de)

Siebenmorgen, R., Heymann, F., & Efstathiou, A. 2015, A&A, 583, A120, doi: [10.1051/0004-6361/201526034](https://doi.org/10.1051/0004-6361/201526034)

Smit, R., Bouwens, R. J., Labb  , I., et al. 2014, ApJ, 784, 58, doi: [10.1088/0004-637X/784/1/58](https://doi.org/10.1088/0004-637X/784/1/58)

Steidel, C. C., Giavalisco, M., Pettini, M., Dickinson, M., & Adelberger, K. L. 1996, ApJL, 462, L17, doi: [10.1086/310029](https://doi.org/10.1086/310029)

Su  rez, G., & Metchev, S. 2022, MNRAS, 513, 5701, doi: [10.1093/mnras/stac1205](https://doi.org/10.1093/mnras/stac1205)

Tacchella, S., Eisenstein, D. J., Hainline, K., et al. 2023, ApJ, 952, 74, doi: [10.3847/1538-4357/acdbc6](https://doi.org/10.3847/1538-4357/acdbc6)

Tremonti, C. A., Heckman, T. M., Kauffmann, G., et al. 2004, ApJ, 613, 898, doi: [10.1086/423264](https://doi.org/10.1086/423264)

Tsai, C.-W., Eisenhardt, P. R. M., Wu, J., et al. 2015, ApJ, 805, 90, doi: [10.1088/0004-637X/805/2/90](https://doi.org/10.1088/0004-637X/805/2/90)

Vanden Berk, D. E., Richards, G. T., Bauer, A., et al. 2001, AJ, 122, 549, doi: [10.1086/321167](https://doi.org/10.1086/321167)

Wang, T., Schreiber, C., Elbaz, D., et al. 2019, Nature, 572, 211, doi: [10.1038/s41586-019-1452-4](https://doi.org/10.1038/s41586-019-1452-4)

Williams, C. C., Alberts, S., Ji, Z., et al. 2023a, arXiv e-prints, arXiv:2311.07483, doi: [10.48550/arXiv.2311.07483](https://doi.org/10.48550/arXiv.2311.07483)

Williams, C. C., Tacchella, S., Maseda, M. V., et al. 2023b, ApJS, 268, 64, doi: [10.3847/1538-4365/acf130](https://doi.org/10.3847/1538-4365/acf130)

Wilson, G., Huang, J. S., Pérez-Gonz  lez, P. G., et al. 2004, ApJS, 154, 107, doi: [10.1086/422716](https://doi.org/10.1086/422716)

Woo, J.-H., & Urry, C. M. 2002, ApJ, 579, 530, doi: [10.1086/342878](https://doi.org/10.1086/342878)

Wright, G. S., Rieke, G. H., Glasse, A., et al. 2023, PASP, 135, 048003, doi: [10.1088/1538-3873/acbe66](https://doi.org/10.1088/1538-3873/acbe66)

Yan, H., Dickinson, M., Eisenhardt, P. R. M., et al. 2004, ApJ, 616, 63, doi: [10.1086/424898](https://doi.org/10.1086/424898)

Zavala, J. A., Buat, V., Casey, C. M., et al. 2023, ApJL, 943, L9, doi: [10.3847/2041-8213/acacfe](https://doi.org/10.3847/2041-8213/acacfe)

Table 1. SED fitting properties for different redshift solutions.

Redshift	Parameter	Codes				
		sy-AGN	LP++	CIG	BP-SF	BP-AGN
$z = 0.4$	$\log(M/M_\odot)$	5.1	5.1	4.8	5.8	5.8
	SFR [$M_\odot \text{yr}^{-1}$]	< 0.1	< 0.1	< 0.1	< 0.1	< 0.1
	Av [mag]	7.7	2.1	3.4	7.4	7.3
	\bar{t}_{M-w} [Myr]	2	126	50	1003	1023
	$\log(L_{\text{IR}}/L_\odot)$	7.8	8.2	6.9	7.0	6.9
comments		$M_{\text{dust}} = 10^{3.2} M_\odot$				
$z = 4.0$	$\log(M/M_\odot)$	8.1	8.4	8.1	7.1	8.0
	SFR [$M_\odot \text{yr}^{-1}$]	200	1.0	12	0.1	0.3
	Av [mag]	4.4	6.2	6.9	2.8	6.2
	\bar{t}_{M-w} [Myr]	5	50	5	10	320
	$\log(L_{\text{IR}}/L_\odot)$	$10^{10.6}$	8.3	10.8	9.2	9.3
comments		$M_{\text{dust}} = 10^{7.1} M_\odot$				
$z = 15$	$\log(M/M_\odot)$	7.2	9.4	8.8	8.3	6.8
	SFR [$M_\odot \text{yr}^{-1}$]	20	30.2	13	2	< 0.1
	Av [mag]	0.2	2.1	2.8	1.1	4.5
	\bar{t}_{M-w} [Myr]	1.0	128	50	60	50
	$\log(L_{\text{IR}}/L_\odot)$	-	8.0	11.0	9.7	9.8
comments		$L_{\text{bol}}^{\text{AGN}} = 10^{44.6} \text{ erg s}^{-1}$		$M_{\text{dust}} = 10^{7.3} M_\odot$		

NOTE—The table shows physical properties (listed in the second column) of the *Cerberus* Galaxy (assuming the source is such) for 3 different photometric redshift solutions (provided in the first column) and 6 different codes and fitting techniques: SYNTHESIZER-AGN (sy-AGN), LEPHARE++ (LP++), CIGALE (CIG), BAGPIPES STAR FORMATION (BP-SF), BAGPIPES AGN (BP-AGN), and prospector (PR). We do not provide nominal uncertainties given that they are much larger than the scatter among the different codes. See main text for details of each modeling procedure. The quoted physical properties are the stellar mass, SFR, stellar light attenuation in the V -band, mass-weighted stellar age, and total infrared luminosity (integrated between 8 and 1000 μm). We also provide the bolometric luminosity of the AGN for the $z = 15$ solution.